Atmos. Chem. Phys. Discuss., 9, 16607–16682, 2009
www.atmos-chem-phys-discuss.net/9/16607/2009/

Atmospheric Chemistry and Physics Discussions

This discussion paper is/has been under review for the journal *Atmospheric Chemistry and Physics (ACP)*. Please refer to the corresponding final paper in *ACP* if available.

Cirrus clouds in a global climate model with a statistical cirrus cloud scheme

M. Wang[1,*] **and J. E. Penner**[1]

[1]Department of Atmospheric, Oceanic, and Space Sciences, University of Michigan, USA
[*]now at: Pacific Northwest National Laboratory, Richland, Washington, USA

Received: 18 June 2009 – Accepted: 30 July 2009 – Published: 7 August 2009

Correspondence to: M. Wang (minghuai.wang@pnl.gov)

Published by Copernicus Publications on behalf of the European Geosciences Union.

Abstract

A statistical cirrus cloud scheme that accounts for mesoscale temperature perturbations is implemented into a coupled aerosol and atmospheric circulation model to better represent both cloud fraction and subgrid-scale supersaturation in global climate models. This new scheme is able to better simulate the observed probability distribution of relative humidity than the scheme that was implemented in an older version of the model. Heterogeneous ice nuclei (IN) are shown to affect not only high level cirrus clouds through their effect on ice crystal number concentration but also low level liquid clouds through the moistening effect of settling and evaporating ice crystals. As a result, the change in the net cloud forcing is not very sensitive to the change in ice crystal concentrations associated with heterogeneous IN because changes in high cirrus clouds and low level liquid clouds tend to cancel. Nevertheless, the change in the net radiative flux at the top of the atmosphere due to changes in IN is still large because of changes in the greenhouse effect of water vapor caused by the changes in ice crystal number concentrations. Changes in the magnitude of the assumed mesoscale temperature perturbations by 25% alter the ice crystal number concentrations and radiative fluxes by an amount that is similar to that from a factor of 10 change in the heterogeneous IN number concentrations.

1 Introduction

Cirrus clouds cover about 30% of the Earth's area (Wang et al., 1996; Rossow and Schiffer, 1999; Wylie and Menzel, 1999) and are important in maintaining the global radiation balance (Ramanathan and Collins, 1991). They can form through either homogeneous freezing or heterogeneous freezing. Homogeneous freezing occurs through the freezing of liquid solutions such as sulfate droplets (Koop et al., 2000), and this usually occurs at low temperature and high relative humidity over ice (RHi). In contrast, heterogeneous freezing is mediated by insoluble solids (Pruppacher and Klett,

ACPD

9, 16607–16682, 2009

1997) or surfactant layers (Zobrist et al., 2007) that lower the energy barrier for the formation of an ice germ, and therefore requires lower supersaturation and can occur at higher temperatures. Aerosol particles that contribute such surfaces and undergo heterogeneous freezing are termed ice nuclei (IN). Mineral dust, carbonaceous, and metallic particles appear to be common heterogeneous IN (Chen et al., 1998; DeMott et al., 2003; Cziczo et al., 2004, 2009).

Homogeneous freezing is believed to be the primary mechanism for cirrus cloud formation in cold environments with high updraft velocities (e.g., Heymsfield and Sabin, 1989; Cantrell and Heymsfield, 2005), but the presence of heterogeneous IN can decrease the occurrence of homogeneous freezing because of the consumption of water vapor that prevents the formation of the high RH*i* needed (e.g., Demott et al., 1997; Liu and Penner, 2005). This preventive effect may significantly change cirrus cloud properties and humidity in the upper troposphere. Heterogeneous freezing from a few IN may result in lower ice crystal number concentrations and larger ice crystal particles than those from homogeneous freezing, since homogeneous freezing usually generates high concentrations of ice crystals because of the abundance of liquid haze particles. Jensen et al. (2008) suggested that it is likely that the observed presence of rather large ice crystals near the tropical tropopause in very low concentrations results from ice nucleation on effective heterogeneous IN. Heterogeneous freezing may also change the frequency of occurrence of cirrus clouds because of the lower RH*i* and thus its more frequent occurrence (Jensen and Toon, 1997). Haag and Kärcher (2004) used a Lagrangian microphysical aerosol-cloud model to show that the frequency of occurrence of thin cirrus clouds can be changed significantly as a result of the presence of a small number of IN at midlatitudes. Heterogeneous freezing may also change ice water content by changing ice crystal settling velocities (e.g., Haag and Kärcher, 2004) and may change humidity fields in the upper troposphere. Haag et al. (2003) suggested that the difference in the probability distribution of relative humidity between the Southern Hemisphere (SH) and the Northern Hemisphere (NH) observed during the Interhemispheric Differences in Cirrus Properties from Anthropogenic Emissions

ACPD
9, 16607–16682, 2009

(INCA) field experiments could be explained by heterogeneous freezing from the increased number of aerosol particles that act as IN in the NH.

The calculation of the effect of heterogeneous IN on cirrus cloud properties is complicated by the fact that small scale dynamical processes play an important role in ice nucleation in the upper troposphere (e.g., Heymsfield, 1977; Ström et al., 1997; Kärcher and Ström, 2003; Haag and Kärcher, 2004; Jensen and Pfister, 2004; Hoyle et al., 2005). Small scale dynamical processes control the cooling rates within parcels that form cirrus clouds, which, together with the ambient temperature determines whether heterogenous or homogeneous freezing dominates the ice nucleation process. Heymsfield (1977) found that the ice crystal concentration and ice water content in cirrus clouds are strong functions of the vertical velocity based on airborne measurements in the United States. Ström et al. (1997) demonstrated the potential impact of atmospheric waves on the physical properties of young cirrus clouds from airborne measurements over Southern Germany. Immler et al. (2008) found a clear correlation between temperature anomalies induced by equatorial Kelvin waves and the occurrence of thin cirrus at the tropical tropopause. The strong role of small scale dynamical processes on ice nucleation and cirrus cloud microphysical properties make it difficult to separate the effects of aerosol changes and dynamical changes on cirrus microphysical properties (Kärcher and Ström, 2003). It has been suggested that cirrus formation is at least as sensitive to changes in dynamical forcing patterns as to changes in the aerosol size and number (Kärcher and Ström, 2003).

Global models have been used recently to study the effect of homogeneous and heterogeneous freezing on cirrus cloud properties (Lohmann and Kärcher, 2002; Hendricks et al., 2005; Liu et al., 2009). In these studies, the individual GCMs were updated to allow supersaturation with respect to ice, but cloud fraction was still diagnosed based on grid-mean relative humidity and equal humidity both inside and outside of cirrus clouds was assumed. This leads to a cloud fraction that is either 0 (if ice nucleation does not occur, and if ice crystals have not formed in the previous time step) or 1 (if ice crystals formed in the previous time step) when the grid mean RH$_i$ is larger than

ACPD
9, 16607–16682, 2009

100%. Partial cloud cover is only diagnosed when subsaturation subsequently occurs. The representation of subgrid-scale fluctuations of temperature, humidity, and cooling rates that are believed to control the cirrus cloud microphysical formation process and the related microphysical cirrus cloud properties, are highly simplified in these studies. The simulated effects of subgrid-scale fluctuations are only represented in the calculation of ice crystal number concentrations while the cloud fraction changes depend only on the grid-mean relative humidity. The simplifications in these models limit their capability to study aerosol indirect effects on cirrus clouds.

To address the inconsistency between the diagnosis of cloud fraction and the prediction of ice supersaturation, Tompkins et al. (2007) used a prognostic cloud fraction that is consistent with their predicted ice supersaturation in the European Centre for Medium-Range Weather Forecasts (ECMWF) Integrated Forecast System. This scheme uses clear sky relative humidity to determine when ice freezing occurs and how much cloud fraction increases. However, this scheme has highly simplified ice microphysics (no ice crystal number is predicted). Moreover, this study assumed vapor saturation in cloudy air. In observations, both ice supersaturation and subsaturation conditions can occur in cloudy air (Ström et al., 2003). For example, significant supersaturation can occur when ice crystal number concentration is low (Krämer et al., 2009), and subsaturation can occur when ice crystal particles are large (Hall and Pruppacher, 1976).

Kärcher and Burkhardt (2008, hereafter KB08) presented a statistical cloud scheme for non-convective cirrus formed by homogeneous freezing of supercooled aerosols, which treats cloud growth and decay based on a subgrid-scale distribution of temperature and total water. The scheme is based on separate probability distribution functions for total water in the clear-sky and cloudy sky portions of each grid. These distributions are based on in situ observations. Both sub- and supersaturation conditions with respect to ice are allowed to occur in cloud-free air and inside cirrus. This scheme was tested in a box model in KB08, which produced nucleated ice crystal number concentrations and ice crystal sizes in good agreement with observations.

ACPD
9, 16607–16682, 2009

In this study, the cirrus cloud scheme in KB08 is implemented in the updated version of NCAR CAM3 (Liu et al., 2007a, hereafter LIU07) which has been coupled with the LLNL/UMich IMPACT aerosol model (Wang et al., 2009), in order to replace the cirrus cloud treatment in LIU07. We have extended the KB08 scheme to include both homogeneous freezing and heterogeneous freezing. Anvil clouds from convective detrainment are also included and compete for water vapor with large scale cirrus clouds in the clear sky portion of each grid. The coupled model and the implementation of KB08 are presented in Sect. 2, and model results in the case of homogeneous freezing only are shown in Sect. 3. The effects of heterogeneous IN and changes to the assumed probability density function of the subgrid scale temperature perturbations are examined in Sect. 4. Finally, Sect. 5 contains a discussion and conclusions.

2 Model description and set-up of simulations

The fully coupled IMPACT aerosol model and NCAR CAM3 model (Wang et al., 2009) are used in this study. The two model components of the coupled system are concurrently run in MPMD (Multiple Processors Multiple Data) mode to exchange aerosol fields and meteorological fields at each advection time step of the IMPACT model (Wang et al., 2009).

2.1 The IMPACT global aerosol model

In this study, the mass-only version of the Lawrence Livermore National Laboratory (LLNL)/University of Michigan IMPACT model was used, which predicts aerosol mass, but not number (Liu and Penner, 2002). We choose the mass-only version of the IMPACT model instead of the complete aerosol microphysics version used in Wang et al. (2009) because the mass-only version of the model is computationally fast which allowed us to run more sensitivity studies.

The mass-only version of IMPACT includes prognostic variables for sulfur and re-

ACPD
9, 16607–16682, 2009

lated species: dimethylsulfide (DMS), sulfur dioxide (SO_2), sulfate aerosol (SO_4^{2-}), and hydrogen peroxide (H_2O_2); aerosols from biomass burning black carbon (BC) and organic matter (OM), fossil fuel BC and OM, natural OM, aircraft BC (soot), mineral dust, and sea salt are also included. Sulfate aerosol is divided into three size bins with radii varying from 0.01–0.05 μm, 0.05–0.63 μm and 0.63–1.26 μm, while mineral dust and sea salt are predicted in four bins with radii varying from 0.05–0.63 μm, 0.63–1.26 μm, 1.26–2.5 μm, and 2.5–10 μm. Carbonaceous aerosol (OM and BC) is currently represented by a single submicron size bin. Emissions of primary particles and precursor gases, gas-phase oxidation of precursor gases, aqueous-phase chemistry, rain-out and washout, gravitational settling, and dry deposition are treated. The mass-only version of the IMPACT aerosol model driven by meteorological fields from the NASA Data Assimilation Office (DAO) participated in the AEROCOM (http://nansen.ipsl.jussieu.fr/AEROCOM/) phase A and B evaluations (Kinne et al., 2006; Textor et al., 2006; Schulz et al., 2006), where it has been extensively compared with in situ and remotely sensed data for different aerosol properties.

Emissions of aerosol species and their precursors are described in detail in Wang et al. (2009). Anthropogenic sulfur emissions were from Smith et al. (2001, 2004), for the year 2000 (61.3 Tg S per year). Anthropogenic emissions of fossil fuel and biomass burning carbonaceous aerosols were from Ito and Penner (2005) for the year 2000, but adjusted as discussed in Wang et al. (2009). The fossil fuel BC and OM emissions were 5.8 Tg BC and 15.8 Tg OM per year, and the biomass burning BC and OM emissions were 4.7 Tg BC and 47.4 Tg OM per year. Emissions of BC from aircraft were 0.0034 Tg per year based on the fuel use model of Lee et al. (2005) with emission factors from AERO2K (Eyers et al., 2004). Natural emissions included volcanic SO_2 (4.79 Tg S per year from Andres and Kasgnoc, 1998), marine dimethyl sulfide (DMS) (26.1 Tg S per year from Kettle and Andreae, 2000), OM from vegetation (14.5 Tg per year from Penner et al., 2001), and mineral dust provided by P. Ginoux (personal communication, 2004) for the year 1998 based on the algorithm of Ginoux et al. (2001). Sea salt emissions (around 2560 Tg per yr) were calculated online in the coupled CAM/IMPACT

ACPD
9, 16607–16682, 2009

model using the method defined in Gong et al. (1997).

Prescribed size distributions from observations were used to calculate the number concentrations of sulfate, dust and soot particles that are used in the ice particle nucleation parameterization described in Sect. 2.2. Sulfate particles were assumed to have a lognormal size distribution with a mode radius of 0.02 μm and a geometric standard deviation of 2.3 (Jensen et al., 1994). For soot particles emitted from the Earth's surface (i.e., biomass burning and fossil fuel combustion), we assumed a size distribution with a mode radius of 0.07 μm and a geometric standard deviation of 1.5 (Pueschel et al., 1992). Aircraft soot has a much smaller size with a mode radius of 0.023 μm and a geometric standard deviation of 1.5 (Petzold and Schröder, 1998). The size distribution of dust particles (Table B1) is taken from De Reus et al. (2000).

2.2 NCAR CAM3

The NCAR Community Atmospheric Model (CAM3) is part of the Community Climate System Model 3 (CCSM3; Collins et al., 2006a, b). The model predicts both cloud liquid water and cloud ice water (Boville et al., 2006). Cloud condensate detrained from deep and shallow convection is added into stratiform clouds. The gravitational settling as well as large-scale transport of cloud condensate is separately treated for cloud liquid and ice (Boville et al., 2006). However, in the standard CAM3, the partitioning between cloud liquid and cloud ice depends only on temperature (T), and both the cloud droplet number and ice crystal number used in the cloud microphysics scheme are prescribed. Therefore, CAM3 is not able to represent a variety of processes (e.g., the Bergeron-Findeisen process, ice nucleation, droplet nucleation) that are important to the study of aerosol-cloud interactions.

The standard CAM3 version was updated in LIU07, by introducing a two-moment cloud microphysics scheme for ice cloud, in which cloud ice number concentrations are predicted by a prognostic equation. The two-moment scheme treats ice nucleation, coagulation, evaporation, and melting. LIU07 also has a more physically-based representation of the liquid/ice partitioning in mixed-phase clouds than that used in the

ACPD
9, 16607–16682, 2009

standard version of CAM3. This is accomplished by explicitly treating the liquid mass conversion to ice due to the depositonal growth of cloud ice at the expense of liquid water (the Bergeron-Findeisen process) using the scheme of Rotstayn et al. (2000). This replaces the simple temperature-dependent liquid/ice partitioning in the standard CAM3. The cloud condensation and evaporation (C-E) scheme of Zhang et al. (2003) in the standard CAM3 is used only for liquid water in warm ($T>0^{\circ}$C) and mixed-phase (-35°C$<T<0^{\circ}$C) clouds, which removes any supersaturation above that of liquid water. Vapor deposition and sublimation of cloud ice is treated based on Rotstayn et al. (2000). With these modifications, supersaturation over ice is allowed in the upper troposphere. The coupled model with the ice cloud treatment in LIU07 has been used to study the effects of aerosols on cirrus clouds (Liu et al., 2009).

In LIU07, although supersaturation with respect to ice is allowed, cirrus cloud fraction is still diagnosed based on the grid-mean relative humidity, as described in Rasch and Kristjánsson (1998). This leads to an inconsistency between increases in cirrus cloud fraction and new cloud formation by ice nucleation. For example, new cloud formation by ice nucleation requires an RH*i* of about 125% (heterogeneous freezing) or 150% (homogeneous freezing), but the cloud fraction in LIU07 begins to increase at an RH*i* of 90%. This causes a large increase in the cirrus cloud fraction in LIU07 (56.8%) compared to the standard CAM3 (32.2%). Moreover, the grid-mean saturation ratio was used to initiate the parameterization of homogeneous freezing or heterogeneous freezing in LIU07, although mesoscale motions such as gravity waves were accounted for using a sub-grid variation of the updraft. Here, in order to treat cirrus cloud formation in a consistent manner in the upper troposphere, the statistical cirrus cloud scheme presented in KB08 was implemented in CAM3, replacing the cirrus cloud treatment of LIU07. This new scheme has subgrid-scale features for clear sky temperature and in-cloud total water, and is more realistic since it captures more of the sub-grid scale physics. Below we describe how the new scheme is incorporated into CAM3. Some important formulas other than those listed in this section appear in Appendix A, and readers are referred to KB08 for more details.

ACPD
9, 16607–16682, 2009

In the new cirrus cloud scheme, the specific humidity in both the clear sky areas (q_{ve}) and cloudy areas (q_{vc}) within a grid is predicted in the model. The specific humidity in the clear sky area is used to determine whether ice nucleation occurs and how much cloud fraction will increase as a result of any freezing, while the specific humidity in the cloudy part of the grid box is used to determine whether vapor deposition or evaporation occurs and is used to determine how much cloud fraction decreases in the case of evaporation. The grid mean specific humidity (q_v) is calculated as $aq_{vc}+(1-a)q_{ve}$, where a is the cloud fraction.

Cloud growth is determined by the mean specific humidity in the clear part of a grid box using an assumed subgrid variation in the temperature profile. As shown in previous studies (KB08; Hoyle et al., 2005; Kärcher and Ström, 2003; Haag and Kärcher, 2004; Jensen and Pfister, 2004), the use of large scale temperature fluctuations alone is not sufficient for ice nucleation in cirrus clouds, and mesoscale temperature fluctuations from small scale motions such as gravity waves are critical to cirrus cloud generation and to the determination of cirrus cloud properties. These mesoscale temperature fluctuations cover horizontal length-scales 1–100 km (Ström et al., 1997; Bacmeister et al., 1999) and arise from a variety of sources. These sources include intense gravity waves released by mesoscale convective systems, high amplitude lee waves induced by high mountain ridges, or high amplitude lee waves induced in the area of jet streams and storm tracks (KB08). Even away from main source areas, there appears to be a persistent background of mesoscale temperature fluctuations driven by mesoscale gravity waves (Gary, 2006, 2008).

In the new cirrus cloud scheme, a probability density function (PDF) of temperature is used to represent mesoscale temperature perturbations in the clear sky portion of a grid. The PDF of temperature (dP_T/dT) is assumed to be a constrained normal distribution with a mean temperature (T_0) that is predicted by the GCM, and a standard deviation of δT that is prescribed (see Eq. (A1) in Appendix A). This normal distribution was shown to be an excellent approximation to the mesoscale distribution of temperature in background conditions in the middle latitudes of both hemispheres (KB08). The

ACPD
9, 16607–16682, 2009

PDF of the temperature distribution is then transformed into a PDF of the saturation ratio (S) (dP_S/dS) (Eq. A2) using the saturation vapor pressure over pure hexagonal ice (Murphy and Koop, 2005) and the mean specific humidity in the clear sky part of the grid (q_{ve}). By comparing the PDF of S with the freezing threshold saturation ratio (S_{cr}), we can determine the portion of the distribution that is located above S_{cr} as:

$$f(S > S_{cr}) = \int_{S_{cr}}^{S_{3+}} \frac{dP_S}{dS} dS, \quad (1)$$

where S_{3+} is the upper bound of the saturation ratio over which dP_S/dS is defined (see Eq. A2). Ice crystals form when dPs/dS extends above the freezing threshold. After taking account of the clear sky fraction ($1-a$), we have cloud fraction increases from ice nucleation defined as

$$\Delta a = (1 - a) f(S > S_{cr}). \quad (2)$$

The increase in the grid-mean ice crystal number concentration (n_i) from ice nucleation is then

$$\Delta n_i = N_i \Delta a, \quad (3)$$

where N_i is the in-cloud ice crystal number concentration from homogeneous freezing and/or heterogeneous freezing. When both homogeneous freezing and heterogeneous freezing is allowed, if S is greater than the critical saturation ratio for heterogeneous freezing, but lower than that required for homogeneous freezing, then N_i is determined by the number of heterogeneous nuclei. If S is greater than the critical saturation ratio for homogeneous freezing, then Ni is set to the sum of the heterogeneous nuclei plus the homogeneous nuclei, as discussed in detail later (Eqs. 6–9).

To calculate N_i, vertical velocities or cooling rates are needed, and are parameterized based on the probability distribution for δT. The mean cooling rate ϖ, induced by mesoscale temperature fluctuations, is approximated by

$$\varpi[K\,h^{-1}] = 8.2\delta T[K], \quad (4)$$

ACPD
9, 16607–16682, 2009

as in Hoyle et al. (2005); then the mean vertical velocity ($\bar{w}$) is deduced by assuming that the cooling takes place in a parcel lifting adiabatically. This cooling rate or vertical velocity is then used to calculate the ice crystal number concentration. For homogeneous freezing, the resulting ice crystal number density N_{i_homo} is approximated as

$$N_{i\_\mathrm{homo}} \approx 2n(\bar{w}), \quad (5)$$

where $n(\bar{w})$ is the ice crystal number concentration from the homogeneous freezing parameterization for the vertical velocity, $\bar{w}$. This formula is based on the integration of the PDF of vertical velocity or cooling rate, and takes account of the following two factors: (a) most of the small cooling rates do not contribute to freezing on average, and (b) high ice crystal concentrations resulting from high cooling rates are more effective at suppressing subsequent supersaturation (KB08).

KB08 demonstrated that a δT of 1 K reproduces the observed distribution of saturation ratios at temperatures near 225 K, as measured in the middle latitudes of both hemispheres from INCA field data (Kärcher and Ström, 2003; KB08). A δT of 1 K is also close to the average mesoscale temperature amplitudes associated with mean mesoscale altitude displacements of air parcels of ∼100 m as inferred from analysis of Microwave Temperature Profiler data by Gary (2006, 2008), who analyzed data from more than 4000 aircraft flight hours taken in the altitude range 7–22 km and with a variety of underlying topography, spanning the latitude range 70° S to 80° N. Gary (2006) also showed that the mesoscale temperature amplitudes increase with altitude, which is consistent with the gravity wave theory (Fritts and Alexander, 2003).

By using Eq. (4), a δT of 1 K gives a cooling rate of 8.2 K/hour and a vertical velocity of 23 cm/s, which is close to the mean vertical velocity of 26 cm/s measured in the updraught regions in the INCA campaign (Kärcher and Ström, 2003). However, it is not known whether the mean updraft velocity of 23 cm/s is representative at other temperatures and at other locations. It is most likely that this mean mesoscale vertical velocity is not applicable for all locations and all temperatures, given the fact that a variety of mechanisms are responsible for mesoscale fluctuations. One issue is that the

ACPD
9, 16607–16682, 2009

use of this velocity causes ice crystal number concentrations that are too high at low temperatures. For example, a vertical velocity of ~20 cm/s would predict an ice crystal number concentration of order 10 cm^{-3} at a temperature of 193 K from homogeneous freezing for a sulfate particle number concentration of 50 cm^{-3}, but such high ice crystal number concentrations at these temperatures are not supported by field observations. Krämer et al. (2009) examined aircraft in-situ observations of ice crystal number concentration from 28 flights in tropical, midlatitude, and Arctic field experiments in the temperature range of 183–250 K and showed that ice crystal number concentrations decreased with decreasing temperature. This decrease in ice crystal number concentrations cannot be reproduced if a constant vertical velocity perturbation is assumed when homogeneous freezing dominates at these levels. A vertical velocity as low as 1 cm/s is able to explain the observed ice crystal number concentrations at very low temperatures, however. Although a decrease in ice crystal number concentrations might also be achieved by changing the number of heterogeneous IN with temperature, we note that vertical velocities of around 1 cm/s were used in Khvorostyanov et al. (2006) and Jensen et al. (2008), and that these were able to reproduce the observed ice crystal number concentration for thin tropopause cirrus from homogeneous freezing during the 2004 CRYSTAL-FACE and 2006 CRAVE campaigns, respectively. Thus, we assumed a linear decrease in the vertical velocity fluctuation with decreasing temperature from 23 cm/s at 238 K to 1.2 cm/s at 193 K and a constant velocity outside these extremes. This results in a mesoscale temperature perturbation of 1 K at 238 K and 0.05 K at 193 K (or below) using Eq. (4).

In KB08, homogeneous freezing is the only freezing mode for cirrus clouds. In this study, an additional scenario that allows competition between homogeneous and heterogeneous freezing is included. When homogeneous freezing is the only freezing mode, ice crystal number concentration from ice freezing (N_{i_homo}) and the threshold freezing saturation ratio (S_{cr_homo}) are parameterized based on Liu and Penner (2005), and are used in Eqs. (2) and (3) (with N_{i_homo} adjusted by a factor of 2, see Eq. 5) to calculate increases in cloud fraction and the grid-mean ice crystal number concentra-

ACPD
9, 16607–16682, 2009

tion. In the scenario where competition between homogeneous freezing and heterogeneous freezing is allowed, S_{cr_homo} and the adjusted N_{i_homo} (Eq. 5) are still used to determine the increase in cloud fraction and ice crystal number concentration due to homogeneous freezing. But when the heterogeneous IN number concentration (N_{in}) exceeds the threshold IN number concentration (N_{in_cr}) derived in Gierens (2003), heterogeneous freezing is allowed. The heterogeneous freezing threshold saturation ratio (S_{cr_hete}) and ice crystal number concentration from heterogeneous ice freezing (N_{i_hete}) are parameterized based on Liu and Penner (2005) and then used to calculate the total cloud fraction increase and the change in ice crystal number concentration from heterogeneous freezing. The ice number from heterogeneous freezing is not multiplied by a factor of 2, since the factor of 2 applied for homogeneous freezing is primarily used to account for the nonlinear dependence of ice crystal number concentrations on vertical velocity. The number of ice crystals formed from heterogeneous freezing is not as sensitive to changes in vertical velocity as those from homogeneous freezing. For example, at temperature 225 K, when vertical velocities increase from 10 cm/s to 50 cm/s, heterogeneous ice crystal number concentrations that are parameterized based on Liu and Penner (2005) change very little for a soot number concentration less than 0.1 cm^{-3}, while homogeneous ice crystal number concentrations increase from 0.20 cm^{-3} to 2.50 cm^{-3} for a sulfate particle number concentration of 50 cm^{-3}. So, the cloud fraction increase and ice crystal number concentration increase in the scenario with both homogeneous and heterogeneous freezing was defined as:

$$\Delta a = (1 - a) f(S > S_{cr\_homo}), \quad (6)$$

$$\Delta n_i = N_{i\_homo} \Delta a, \text{ when } N_{in} < N_{in\_cr} \quad (7)$$

and

$$\Delta a = (1 - a) f(S > S_{cr\_hete}), \quad (8)$$

$$\Delta n_i = N_{i\_hete} \Delta a + N_{i\_homo}(1 - a) f(S > S_{cr\_homo}), \text{ when } N_{in} > N_{in\_cr}. \quad (9)$$

ACPD
9, 16607–16682, 2009

where N_{i_homo} (increased by a factor of 2, see Eq. 5) and N_{i_hete} are evaluated at the average updraft velocity $\bar{w}$.

In the treatment with both homogeneous freezing and heterogeneous freezing, heterogeneous freezing is only allowed to occur when the concentration of heterogeneous IN exceeds the critical heterogeneous IN concentration. However, in the real atmosphere, when the saturation ratio exceeds the freezing threshold saturation ratio, heterogeneous freezing occurs once heterogeneous IN are present, regardless of the concentration of the heterogeneous IN. This implies that Eqs. (8) and (9) should always be applied when the saturation ratio is larger than the freezing threshold saturation ratio. But given the large time step used in the NCAR CAM3 (30 min), the application of Eqs. (8) and (9) without a limitation set by the number of heterogeneous IN concentrations would significantly decrease supersaturation levels in the model and result in very few homogeneous freezing events even when the concentration of heterogeneous IN is very low (<1/L). So in our treatment (and that by Liu et al., 2009), the competition between homogeneous freezing and heterogeneous freezing is partially parameterized by using the critical heterogeneous IN concentration. When the heterogeneous IN concentration is lower than the critical heterogeneous IN concentrations, heterogeneous freezing will not occur and the heterogeneous IN concentration is assumed to have no effect on homogeneous freezing.

Parcel model results may be used to quantify how accurate the treatment given in Eqs. (6–9) is. Liu and Penner (2005) showed that when the heterogeneous IN concentration is larger than N_{in_cr}, the ice crystal number concentration is determined by heterogeneous freezing. There is a transition region for heterogeneous IN number concentrations from $N_{in\_cr}/10$ to N_{in_cr}, in which ice crystal number concentrations gradually decrease from those determined by homogeneous freezing to those determined by heterogeneous freezing. When heterogeneous IN concentration are lower than $N_{in\_cr}/10$, ice crystal number concentrations are determined by homogeneous freezing. Compared with the results from the parcel model in Liu and Penner (2005), our treatment is reasonable for low IN concentrations ($<N_{in\_cr}/10$) and for high IN con-

ACPD
9, 16607–16682, 2009

centrations ($>N_{in\_cr}$). However, when the concentration of heterogeneous IN is in the transition region (from $N_{in\_cr}/10$ to N_{in_cr}), heterogeneous freezing is not allowed in our treatment, and ice crystal number concentration is determined by homogeneous freezing. Ice crystal number concentrations may then be overestimated, and biased toward the ice crystal number concentration given by homogeneous freezing.

Here we use the critical heterogeneous IN concentration derived by Gierens (2003) to determine whether heterogeneous freezing will occur. In this formulation, the threshold IN number concentration (N_{in_cr}) is a function of S_{cr_homo}, S_{cr_hete}, vertical velocity, temperature, and pressure (Gierens, 2003). Liu and Penner (2005) obtained a similar formula by empirically fitting N_{in_cr} as a function of vertical velocity from their parcel model simulations. As shown in Liu and Penner (2005), the two formulas give similar N_{in_cr} for vertical velocities larger than 20 cm/s. It was further shown by Liu et al. (2009) that simulated changes in cirrus cloud properties and cloud forcing due to anthropogenic aerosols are very similar from these two formulas, when a subgrid scale PDF of vertical velocities with a mean of 0 and a standard deviation of 25 cm/s is used. However, at low vertical velocities (less than 5 cm/s), N_{in_cr} from Liu and Penner (2005) is much smaller than that from Gierens (2003). For example, at 193 K, with a vertical velocity of 1.2 cm/s, N_{in_cr} is 6.13×10^{-6} cm^{-3} in Liu and Penner (2005) and is 6.12×10^{-3} in Gierens (2003). Heterogeneous freezing occurs exclusively at very low vertical velocities when the formula in Liu and Penner (2005) is used. Therefore, the formula of Gierens (2003) is used rather that that of Liu and Penner (2005) mainly because vertical velocities are restricted to low values at low temperatures in this study. The use of the Liu and Penner (2005) values for N_{in_cr} would lead to concentrations of ice crystal number concentrations that are lower than the observations of Krämer et al. (2009) when heterogeneous IN number concentrations are low. The source of heterogeneous IN used in the model is discussed in Sect. 2.3.

An initial ice crystal mass of 10^{-12} kg is assumed for newly formed ice particles. This is a simplification of the treatment used in KB08, where new ice crystal sizes are parameterized based on homogeneous freezing. Because the time step of the

ACPD
9, 16607–16682, 2009

GCM is large (about half an hour), all supersaturation in newly formed clouds is usually removed and the in-cloud saturation ratio with respect to ice is close to 1.0, which makes the initial ice crystal mass less important. After the removal of the initial ice crystal mass, the remaining water vapor in the new clouds is then moved into the cloudy portion of the grid and the in-cloud specific humidity q_{vc} is updated.

In cloudy areas, ice crystals grow through vapor deposition and the in-cloud water vapor q_{vc} is transferred to ice crystals via gas phase diffusion,

$$(\Delta q_{vc})_{\text{dep}} = -(q_{vc} - q_{\text{sat}})\{1 - \exp(-\tau/\tau_s)\}, \quad (10)$$

where q_{sat} is the saturation specific humidity, τ is the time step, and τ_s is the instantaneous relaxation time scale (see Eq. A7), which determines how long the supersaturation (S_{cr}-1) lasts after freezing. The change in the grid averaged ice water content through vapor deposition is $-a(\Delta q_{vc})_{\text{dep}}$.

Cloud decay is determined by the in-cloud specific humidity, ice water content, and a PDF of the in-cloud total water mass mixing ratio (q_{totc}) (see Eq. A9). In-cloud specific humidity has a homogeneously distributed PDF in the form of a delta function, $\delta(q-q_{vc})$. Therefore, the PDF of the total water mass mixing ratio ($dP_{\text{qtot}}/dq_{\text{tot}}$) is determined by the PDF of the in-cloud ice water content (q_i, see Eq. A8). Cloud decay occurs when the in-cloud air becomes subsaturated (in-cloud saturation ratio S_c<1) due to warming or drying. This subsaturation leads to the sublimation of ice crystals. The smallest ice crystals experiencing the highest subsaturations will completely sublimate first. The sublimation (Δq_{vc}) is calculated based on Eq. (10) when q_{vc} is less than q_{sat}. The cloud fraction decrease is determined by the portion of the PDF of ice water in which ice water is less than Δq_{vc}, and is calculated as:

$$\Delta a = a\int_{q_{vc}}^{q_{vc}+\Delta q_{vc}} \frac{dP_{q_{\text{totc}}}}{q_{\text{totc}}} dq_{\text{totc}} = -\text{erf}(\xi)a, \xi = a\Delta q_{vc}/(q_i\pi^{0.5}), \quad (11)$$

where erf*(x)* is the error function (see Eq. A5). The change in ice water content is determined by the following formula:

$$\Delta q_i = -q_i[1 - exp(-\xi^2) + \pi^{0.5}\xi\{1 - \text{erf}(\xi)\}]. \quad (12)$$

ACPD
9, 16607–16682, 2009

The decrease in ice crystal number concentration (Δn_i) is assumed to be proportional to the cloud fraction decrease, and is calculated as

$$\Delta n_i = n_i \Delta a / a. \quad (13)$$

In the standard version of CAM3, detrained cloud water is added to the large scale clouds along with the convective cloud fraction (a_{conv}) which is diagnosed from convective mass fluxes (Boville et al., 2006). This is the case for warm clouds and mixed-phase clouds treated in this study, where cloud droplet and ice crystal number from detrained cloud water are also added into the large scale clouds with assumed volume mean radii (see Appendix B for details). For cirrus clouds, detrained cloud ice mass and crystal number are still added to the large scale clouds in the same way as in warm and mixed-phase clouds. But since cloud fraction in cirrus clouds is prognostic rather than diagnostic, cloud fraction increases from the convective source are calculated at each time step by the following:

$$(\Delta a)_{\text{conv}} = (1 - a) a_{\text{conv}}, \quad (14)$$

The factor $1-a$ in Eq. (14) appears because convective air detrains simultaneously into cloud-free air, as well as into already existing clouds, ensuring realistic limits at zero cloud cover and at cloud cover 1, following the same assumption as in Tiedtke (1993). This new cloud is assumed to be at saturation with respect to ice (the same assumption is used in the standard CAM3, see Boville et al., 2006), which also sets the upper limit of the cloud fraction increase from convective cloud as $(1-a)q_{ve}/q_{\text{sat}}$ (i.e., the water vapor in the new cloud ($(\Delta a)_{\text{conv}} q_{\text{sat}}$) will not exceed the available water vapor in the clear sky $(1-a)q_{ve}$)). After the cloud fraction from convective clouds is updated, the in-cloud specific humidity is calculated as

$$q_{vc} = (q_{vc} a + q_{\text{sat}} (\Delta a)_{\text{conv}}) / (a + (\Delta a)_{\text{conv}}). \quad (15)$$

In the standard CAM3 and the version updated in LIU07, only the grid-mean specific humidity (q) is predicted, using:

$$\frac{\partial q}{\partial t} = A_q - Q + E_r, \quad (16)$$

ACPD
9, 16607–16682, 2009

where A_q is the tendency of water vapor from processes other than large-scale condensation and evaporation of cloud and rain water, Q is the net condensation rate, and E_r is the evaporation of rain water. In order to predict the in-cloud specific humidity (q_{vc}), we assume that A_q is uniformly applied to the whole model grid cell, which is also the assumption made in the condensation-evaporation scheme in CAM3 (Zhang et al., 2003). The in-cloud specific humidity is then predicted together with cloud fraction growth (from both both large scale and convective clouds), decay, and in-cloud vapor deposition/evaporation.

Both cloud ice mass and ice crystal number are advected as in LIU07. As discussed in Boville et al. (2006), advection of cloud condensate is important in the tropical upper troposphere where the mass of ice and vapor phases of water are similar and the lifetime of cloud ice is relatively long. The tendencies of cloud ice mass (A_{qi}) and ice crystal number (A_{ni}) from processes other than large-scale formation or decay of clouds, detrainment, and sedimentation are also assumed to be uniformly applied to the whole model grid cell. It is assumed that the part of these tendencies that falls into the clear sky portion of the grid is evaporated (the same assumption as that used in Zhang et al., 2003). For simplicity, the cloud fraction predicted here is not advected. As a consequence, cloud ice may be advected to grids that have no cloud fraction or partial cloud fraction. If this is the case, the cloud ice that is advected into the clear sky portion of the grid will be evaporated.

In addition to the new cirrus cloud scheme, several other updates have been made in the version of CAM3 used in this study compared with the version used in LIU07. These include a prognostic liquid droplet number equation that takes into account droplet activation, coagulation, evaporation, and freezing, which, together with the ice cloud treatment, consists of a complete set of equations for the two-moment treatment of cloud microphysics in NCAR CAM3. Also the direct conversion from liquid to ice in mixed-phase clouds which was used in simulating observed clouds in the Mixed-Phase Arctic Cloud Experiment (M-PACE) in a single column model (Liu et al., 2007b) and in a short-range weather forecasting approach (Xie et al., 2008) was included. These

ACPD
9, 16607–16682, 2009

updates are described in detail in Appendix B.

2.3 Set-up of simulations and experimental design

The simulations are described in Table 1. In "HOM", only homogeneous freezing on sulfate particles was considered. All other simulations take into account both homogeneous and heterogeneous freezing, but with varied IN concentrations and varied subgrid-scale temperature perturbations.

Three cases are used to study how cirrus cloud properties change with different IN concentrations. The freezing capabilities of different aerosol particles acting as IN are poorly understood. Here we simply use sensitivity tests to study the effects of different aerosols as IN on cirrus clouds. The same temperature perturbation as that used in the HOM case is applied, but with 1%, 10%, and 100% of soot and dust particles acting as heterogeneous IN in HMHT_0.01IN, HMHT_0.1IN, and HMHT_1IN, respectively. The 1% value is consistent with the report by Seifert et al. (2003) that scavenging ratios were <1% in the INCA campaign. The 100% value represents the case where soot and dust particles are efficient IN, as assumed in some previous modeling studies (e.g., Hendricks et al., 2005). Additionally, two cases are used to study how different temperature perturbations will change cirrus cloud properties. These two cases have the same IN concentration as in the HMHT_0.01IN case, but temperature perturbations have been decreased/increased by 25% in HMHT_0.75dT and HMHT_1.25dT, respectively. These results are also compared with the results from the standard version of CAM3 (CAM3) and LIU07. In LIU07, the treatment of ice clouds does not include the subgrid parameterization of supersaturation and cloud fraction used here and the cloud droplet number concentrations in liquid clouds are prescribed as in the standard version of CAM3.

We used 26 vertical levels and a horizontal resolution of 2×2.5 degrees for both the CAM3 and IMPACT models in this study. The time step for CAM3 was 30 min, and the time step for advection in IMPACT was 1 h. The finite volume dynamical core was chosen for CAM3. All simulations used climatological sea surface temperatures. In

ACPD
9, 16607–16682, 2009

each simulation, the coupled model was integrated for 5 years after an initial spin-up time of four months.

3 Model results for the HOM case

Tables 2 and 3 show the annual global mean values for several parameters in our simulations along with results from the standard CAM3 and observations. The liquid water path in the HOM simulation is 77 g/m^2, much less than that simulated in LIU07 and in the standard CAM3, and close to the observed range of 50–84 g/m^2; this value is also close to that simulated by Gettleman et al. (2008) in a modified version of CAM3 that also includes a two moment cloud microphysics treatment (74 g/m^2). The large decrease in liquid water path compared with that in LIU07 is mainly caused by the treatment of the Bergeron-Findeisen process where ice crystals grow at the expense of liquid droplets. As noted above, this treatment has been changed to that of Xie et al. (2008). In the treatment here, a direct conversion from liquid to ice is assumed and the in-cloud vapor pressure that is used to calculate the vapor deposition on ice crystals is the saturation vapor pressure over liquid and ice with each weighted by the proportions of ice and liquid water mass (Xie et al., 2008). In LIU07, the conversion occurs as a result of supersaturation with respect to ice, where the grid-averaged vapor pressure is used to calculate vapor deposition based on Rotstayn et al. (2000). Then the remaining liquid water is evaporated because of subsaturation with respect to liquid water, and further deposition on ice takes place. Because grid-averaged vapor pressure is usually less than the saturation vapor pressure that is weighted by the proportion of ice and liquid water mass, the treatment in LIU07 results in a smaller conversion rate from liquid to ice in mixed-phase clouds than that used in this study (Xie et al., 2008; Appendix B). Because ice crystals are more efficient at producing precipitation, the inclusion of this process in the manner outlined here decreases the liquid water path significantly compared to that in LIU07.

In our simulations, cloud-top quantities (liquid droplet and ice crystal number and

ACPD
9, 16607–16682, 2009

radius) are estimated as seen by satellite instruments using a modification of the maximum/random cloud overlap assumption that is used in the radiative transfer calculations in the NCAR CAM3 (Collins et al., 2001) to obtain the two-dimensional field (Quaas et al., 2004). Cloud top quantities are sampled only for clouds with optical depth larger than 0.3, and are also only sampled once per day at the over pass time of MODIS Aqua satellite (01:30 p.m., local time). For cloud droplet radius, the samples are limited to warm clouds (cloud top temperature larger than 273.16 K), and for ice crystal radius, the samples are limited to cold cirrus clouds (cloud top temperature less than 238.16 K). Using this procedure, our simulated cloud top droplet effective radius for warm clouds (cloud top temperature > 273.16 K) is 11.1 μm, which matches well with AVHRR observations (11.40 μm), but is lower than that from MODIS observations (15.7 μm). The column integrated droplet number concentration averaged over 50° S–50° N is 2.3×10^{10} m^{-2}, and is underestimated compared with AVHRR observations (4.0×10^{10} m^{-2}).

The ice water path is 21 g/m^2, which is comparable to satellite observations (Fig. 18 in Waliser et al., 2009). The column integrated ice crystal number concentration is about 0.022×10^{10} m^{-2}, which is much smaller than that predicted by Lohmann et al. (2007) ($0.1–0.7\times10^{10}$ m^{-2}). The large difference mainly comes from the difference in the treatments of mixed-phase clouds. In our model, deposition/condensation freezing and contact freezing are included in mixed-phase clouds. Deposition/condensation freezing is parameterized based on Meyers et al. (1992) and is a function of ice supersaturation. Mineral dust particles are the only contact freezing ice nuclei. The simulated ice crystal number concentration in mixed-phase clouds is generally less than 1/L, which compares well with observations from the M-PACE field experiments. In Lohmann et al. (2007), both mineral dust and soot particles act as contact freezing ice nuclei. Moreover, Lohmann et al. (2007) included an immersion freezing scheme that has a freezing fraction of 1 for dust particles at temperatures lower than −15°C and has a freezing fraction of 1 for soot particles at temperatures lower than −25°C (Fig. 10 in Phillips et al., 2008), which probably explains why Lohmann et al. (2007)

ACPD
9, 16607–16682, 2009

simulated much higher ice crystal number concentrations than that simulated here for mixed-phase clouds. The average cloud top ice crystal radius for cold cirrus clouds (cloud top temperature less than −35°C) is 39.6 μm, larger than that observed in the MODIS satellite (25.21 μm).

Total cloud fraction is 66% which compares well with the observations. The new cirrus cloud scheme simulates significantly fewer high clouds than LIU07 and improves the model results compared with observations. Shortwave cloud forcing is −52 W/m^2, which is comparable to ERBE (−54 W/m^2) and CERES (−47 W/m^2) observations. Long wave cloud forcing is 28 W/m^2, which is also comparable to ERBE (30 W/m^2) and CERES (29 W/m^2) observations. The precipitation rate is 2.89 mm/day, slightly higher than observations.

Figure 1 shows the annual average zonal mean liquid water path, ice water path, cloud top in-cloud droplet number concentration and droplet effective radius for liquid clouds, cloud top in-cloud ice crystal number and effective radius for cirrus clouds (for cloud top temperatures less than −35°C), shortwave cloud forcing, and longwave cloud forcing. Cloud top droplet number concentrations have a strong north-south contrast with a larger number concentrations in the NH, which is consistent with data derived from MODIS observations (Quaas et al., 2006), and is mainly caused by anthropogenic aerosols in the model. Correspondingly, cloud top droplet effective radius has a larger value in the SH than in the NH, which is consistent with the AVHRR observations (Han et al., 1994). Liquid water path has larger values in the middle latitude storm tracks over both hemispheres, which is consistent with SSM/I data (Ferraro et al., 1996). The ice water path has two peak values in the middle latitudes of both hemispheres, which is consistent with ISCCP observations (Storelvmo et al., 2008). For cirrus clouds, cloud top ice crystal number concentration is large over the tropics and the two polar regions. The ice crystal effective radius has two peaks in the middle latitudes of both hemispheres, with minima in the tropics and the two polar regions. The minima in the tropics is not consistent with MODIS data, which have a larger ice crystal radius in the tropics than that in the middle latitudes. Short wave cloud forcing and long wave cloud

ACPD
9, 16607–16682, 2009

forcing have latitudinal variations that agree with the CERES observations.

Figure 2 shows annual average zonal mean latitude-pressure cross sections for grid-averaged droplet number concentration, liquid water content, ice crystal number concentration, and ice water content. Liquid water content shows two peaks in the storm tracks of both hemispheres, which extend into the middle troposphere. Liquid droplet number concentrations show a similar pattern: two peaks in the middle latitudes in both hemispheres, but the influence of anthropogenic aerosols is also evident: there is a stronger peak in the NH than in the SH. For ice clouds, large ice crystal number concentrations are found over the upper troposphere in tropical regions and at both poles. The simulated grid mean ice crystal number concentrations are comparable to results from Lohmann et al. (2007), except that they simulated higher ice crystal number concentrations in mixed-phase clouds, as mentioned above. Large ice water content can be found in the lower troposphere over high latitudes in both hemispheres and in the upper troposphere in the tropics.

Ice water content (IWC) in the upper troposphere is compared with that from the Microwave Limb Sounder (MLS) onboard the Aura Satellite (Wu et al., 2006) in Fig. 3. The MLS ice water content data have a vertical resolution of ~3.5 km and a horizontal resolution of ~160 km for a single MLS measurement along an orbital track (Wu et al., 2006, 2009). The data used here for comparison are monthly means from September 2004 to August 2005. The model broadly captures the spatial and zonal distribution of ice water content in the upper troposphere, but it underestimates the ice water content in tropical regions by a factor of 2 to 4, which is also true for the standard CAM3 model (Li et al., 2005). The model ice water content is larger at the poles than in MLS data, a feature that is improved when heterogeneous IN are included in the model (see Sect. 4.1.2). We notice that the ice water content simulated in LIU07 is larger in tropical regions than that simulated here and is in better agreement with MLS data, but the reasons for this are not known. The cirrus treatment in this study is different than that in LIU07 in several respects, including the different treatments of cloud growth and cloud decay and formation of ice number concentrations as described above. In

ACPD
9, 16607–16682, 2009

addition, we apply a mean vertical velocity rather than a PDF of vertical velocities, and anvil cloud fraction is added as one source term in the predicted total cloud fraction using Eq. (14) while in LIU07 the total cloud fraction is the sum of the diagnostic large scale cloud fraction and the anvil cloud fraction. These differences make it difficult to attribute differences in the simulated ice water content between this study and that in LIU07 to any of the individual processes. Increasing the temperature variations in our treatment, as is done in Sect. 4.2, does not alleviate this problem.

Figure 4 shows annual average zonal mean latitude-pressure cross sections for the in-cloud ice crystal number concentration from the prognostic ice crystal equation and that simulated immediately after the initial ice nucleation. Ice crystal number concentration from the initial nucleation of ice ranges from 0.5 to 5 cm^{-3}, and slowly increases with decreasing temperature although at very low temperatures it decreases with decreasing temperature (Compare temperature in Fig. 2 with N_{i_homo} in Fig. 4b). The decrease is caused by the low vertical velocity we used at low temperatures (Sect. 2.2). In our treatment, mean vertical velocities linearly decrease from 23 cm/s at 238 K to 1.2 cm/s at 193 K. Based on the homogeneous freezing parameterization of Liu and Penner (2005), ice crystal number concentration from homogeneous freezing is then at its maximum at around 200 K, which explains why ice crystal number concentration decreases with decreasing temperature at very low temperature (lower than 200 K). The ice crystal number concentrations predicted from the prognostic ice crystal equation are lower by a factor of 2 to 5 compared to the initial concentrations predicted after ice nucleation, due to the impact of sublimation, gravitational settling, precipitation removal, and advection. As shown later in Sect. 4, different freezing mechanisms lead to different ice crystal number concentrations in the upper troposphere.

Table 4 compares the simulated ice crystal number concentration from the prognostic ice crystal equation in the HOM model with those measured during the INCA campaign (Gayet et al., 2004). Ice crystal number concentrations were measured in middle latitude cirrus clouds at temperatures ranging from −33°C and −60°C during the INCA campaign over Punta Arenas in the SH (Chile, in March/April) and over Prestwick in the

ACPD
9, 16607–16682, 2009

NH (Scotland, in September/October). Most flight patterns during the campaign were designed to probe young cirrus clouds (Kärcher and Ström, 2003). The measured ice crystal number concentrations in the SH and NH have a median of 1.4 and 2.2 cm^{-3}, respectively (Gayet et al., 2004). Simulated mean ice crystal number concentrations from the prognostic ice crystal equation in the HOM case are 0.34 and 0.33 cm^{-3} in the SH and NH, respectively, and are significantly lower than those observed during the INCA campaign. The INCA observations mainly represented young cirrus clouds, however, and ice crystal number concentrations immediately after the initial ice nucleation from homogeneous freezing (shown in the parenthesis for the HOM case in Table 4), are 1.2 and 1.6 cm^{-3} in the SH and NH, respectively, in better agreement with the INCA observations.

Figure 5 shows in-cloud ice crystal number concentration (ICNC) and ice crystal effective radius (REI) versus temperature. Model results are sampled every six hours over six flight regions (Kiruna, Sweden in January and February; Hohn, Germany in November and December; Forli, Italy in Octorber; Mahe, Seychelles, in February and March; Darwin, Australia, in November; Aracabuta, Brazil in January and February) where the observations reported in Krämer et al. (2009) were collected (See Table 3 in Krämer et al. (2009) for the flight information). The median, 25% percentile, and 75% percentile are shown for each 1 K temperature bin. In-cloud ice crystal number concentrations in the HOM case increase with decreasing temperature (the median ice crystal number concentration is 0.08 cm^{-3} at 230 K and 0.13 cm^{-3} at 200 K), although the vertical velocities used in the model decrease with decreasing temperature. In Krämer et al. (2009) (Fig. 9 in their paper), ice crystal number concentration decreases with decreasing temperature, with a mean value ~0.2 cm^{-3} at 230 K and ~0.1 cm^{-3} at 200 K. Decreasing the vertical velocity with decreasing temperature as treated in our model is still not able to simulate the decreasing ice crystal number concentrations with decreasing temperatures when only homogeneous freezing is included. Simulated ice crystal radius increases with increasing temperature, which is consistent with the results reported in Krämer et al. (2009) (Fig. 9 in their paper), although the ice crystal

ACPD
9, 16607–16682, 2009

radius increases faster with temperature than that in observations.

Figure 6 shows the simulated PDF of RH*i* outside of cirrus clouds within two layers (100–200 hPa, and 200–300 hPa) and in three regions (the SH middle latitudes: 60° S–30° S; the tropics: 30° S–30° N; and the NH middle latitudes: 30° N–60° N). One year of model results are sampled every six hours. The PDF of the clear-sky RH*i* is calculated based on the clear-sky mean RH*i* and the prescribed temperature perturbations used in the model (Sect. 2.2, Eq. A2) weighted by the clear sky fraction (1−*a*). Also shown in Fig. 6 is the PDF of RH*i* from the Measurement of Ozone and Water Vapor by Airbus In-service Aircraft (MOZAIC) campaign (Spichtinger et al., 2004) for the NH middle latitudes and the tropics. MOZAIC data sampled both clear sky and cloudy sky conditions. We only compared the RH*i* in clear sky conditions because the model assumes a uniform distribution for the in-cloud specific humidity and the large time step used in the GCM makes the saturation ratio under cloudy sky conditions very close to 1. In the clear sky, the RH*i* are sampled across the whole PDF spectrum regardless of whether the value of RH*i* exceeds the heterogeneous freezing or homogeneous freezing threshold. By doing this, the in-cloud conditions sampled in the MOZAIC data are partly taken into account in the model data.

The homogeneous freezing-only case (HOM) reproduces the shape of the PDF of RH*i* from MOZAIC data well. RH*i* in the range from 20–100% occurs with large frequency, and the frequency has an almost exponential decay from RH*i*=100% to around RH*i*=150%, a feature that is consistent with the MOZAIC data and is believed to be mainly caused by temperature variations (Kärcher and Haag, 2004). Beyond 150%, the HOM case simulates a faster decay of RH*i* than that in the MOZAIC data. This fast decay in the HOM case is caused by homogeneous ice freezing that has a threshold RH*i* near 150%.

Figure 7 shows the geographical distribution of the frequency of occurrence of ice supersaturation in clear sky regions in the HOM case and from the Microwave Limb Sounder (MLS) satellite data (Spichtinger et al., 2003) at pressure levels 147 hPa (139 hPa is shown for the model) and 215 hPa (192 hPa is shown for the model). The

ACPD
9, 16607–16682, 2009

frequency of occurrence of ice supersaturation for a given grid point is calculated as the number of samples with RHi>100% divided by the total number of samples for a given period (one year in the model, September 1991 to June 1997 for the MLS data), weighted by the clear sky fraction (1−a). In contrast to the comparison with the MOZAIC data, the mean clear-sky RHi instead of the subgrid-scale RHi in the model is used to calculate the ice supersaturation frequency because of the large field view of the MLS measurement (about 100×200 km^2 perpendicular and parallel to the line of sight and 3 km vertically). At the 147 hPa level, the observed ice supersaturation occurs most frequently in the tropics between 20° S and 20° N and over Antarctica. Compared with the MLS data, the model with only homogeneous freezing (HOM) reproduces the observations well in terms of the spatial distribution, but gives a higher ice supersaturation frequency than does the MLS data.

At the 215 hPa level, the observed ice supersaturation occurs most frequently in the same regions as at the 149 hPa level, although the high frequency ice supersaturation regions also extend toward high latitudes at 215 hPa, mainly over the storm track regions in both hemispheres. The model produces a similar spatial distribution as that in the MLS observations but with an even larger overestimation than that at 147 hPa, and the ice supersaturation regions extend even more towards high latitudes in the model. For example, the model simulates a high frequency of ice supersaturation occurrence in the SH storm track (around 45° S), which is not present in the MLS observations. As pointed out by Spichtinger et al. (2003), there are considerable data gaps in the middle latitudes of the summer hemispheres in the MLS data. This may prevent us from drawing further conclusions about whether the simulated ice supersaturation regions over the storm track at the 215 hPa level is reasonable or not. To summarize the model performance regionally, averaged supersaturation frequencies in five regions (global, Northern Hemisphere, tropics, Southern Hemisphere, and Antarctic) in both the MLS data and the model are shown in Fig. 8. This confirms that geographical variations in supersaturation frequency are broadly captured, but with a significant overestimation, especially at 215 hPa, a feature that is improved when heterogeneous IN are included

ACPD
9, 16607–16682, 2009

(Sect. 4.1).

The simulated supersaturation frequencies also depend on the mesoscale temperature perturbations used in the model. A large temperature perturbation produces more ice, which decreases the clear sky relative humidity and decreases the supersaturation frequency simulated in the model. A larger temperature perturbation, then, would improve the comparison with MLS data, especially at 139 hPa, since quite small temperature perturbations were used due to the low temperatures there (Sect. 2.2). Larger mesoscale temperature perturbations at higher altitude is also consistent with gravity wave theory (Fritts and Alexander, 2003) and observations (Gary et al., 2006) although larger vertical velocities resulting from larger temperature perturbations by using Eq. (2) would produce high ice crystal number concentrations that are not supported by field observations, as discussed in Sect. 2.2.

4 Effects of heterogeneous IN and mesoscale temperature perturbations

4.1 Effects of heterogeneous IN

The effects of heterogeneous IN on cirrus cloud properties are studied using three sensitivity tests: HMHT_0.01IN, HMHT_0.1IN, and HMHT_1IN, in which IN concentrations are assumed to be 1%, 10%, and 100% of the total number concentration of BC and dust particles, respectively, as described in Table 1. The annual average zonal mean distributions of dust and BC number concentrations are shown in Fig. 9. BC particles have a high concentration in the NH upper troposphere (100 hPa to 400 hPa) with a range of 1–10 cm^{-3}, caused by the larger anthropogenic emissions in the NH. The number concentrations of BC particles in the upper troposphere decrease with latitude from north to south. In the upper troposphere of the SH, the concentrations range from 0.3 to 1 cm^{-3}. Dust particles are much lower in number concentration and there is a stronger gradient with altitude from the surface to the upper troposphere than for BC particles because of their larger sizes and the lack of a source in the upper tro-

ACPD
9, 16607–16682, 2009

posphere. The number concentrations of dust particles range from 0.001 to 1 cm^{-3} in the NH upper troposphere, and range from 0.001 to 0.03 cm^{-3} in the SH upper troposphere.

4.1.1 Effects on humidity fields

Figure 6 shows the effect of heterogeneous IN on the frequency of occurrence of RH*i*. Heterogeneous IN decrease the frequency of occurrence of very high supersaturations due to their lower threshold RH*i* which is assumed to be between 120–130% in the parameterization of Liu and Penner (2005). Heterogeneous freezing has little effect in the tropics and in the SH when only 1% of soot and dust particles act as IN in the HMHT_0.01IN case, because the IN concentration is too low in these regions to prevent supersaturations high enough to allow homogeneous freezing. However, in the NH middle latitudes, the IN concentration exceeds the critical IN concentration from Gierens (2003), and heterogeneous freezing is allowed to occur. The hemispheric contrast in the PDF of the RH*i* in this case is consistent with that observed in the INCA field campaign (Haag et al., 2003). Heterogeneous freezing occurs more frequently when the IN concentration increases by a factor of 10 in the HMHT_0.1IN case. In the middle latitudes of the NH, heterogeneous freezing shuts off homogeneous freezing, as evidenced by the very low frequency of RH*i* values higher than 150%. In the middle latitudes of the SH, homogeneous freezing still occurs but with a much lower frequency than that in the HMHT_0.01IN case. Homogeneous freezing is shut down almost everywhere in the HMHT_1IN case when 100% of the BC and dust particles act as heterogeneous IN.

The effects of heterogeneous IN can also be seen in the simulated regionally averaged frequency of occurrence of ice supersaturation at 139 hPa and 192 hPa in Fig. 8. When 1% of dust and BC particles act as heterogeneous IN (HMHT_0.01IN), the simulated supersaturation frequencies decrease, with larger decreases over the NH than the SH, and larger decreases at 215 hPa than at 147 hPa because of the higher IN con-

ACPD
9, 16607–16682, 2009

centrations there. For example, at 215 hPa, the simulated supersaturation frequencies in the HOM case and the HMHT_0.01IN case are almost the same in the SH middle latitudes, but decrease from 13% in the HOM case to 5.83% in the HMHT_0.01IN case in the NH middle latitudes. When heterogeneous IN concentrations increase by a factor of 10 in the HMHT_0.1IN case, supersaturation frequencies in all regions and at both 147 hPa and 215 hPa decrease significantly. These model results show that ice microphysics is important for simulating supersaturation frequencies in the upper troposphere. Including heterogeneous IN decreases simulated supersaturation frequencies in the model, and gives a better comparison with the frequencies of supersaturation from the MLS data at 215 hPa. But this conclusion has to be treated cautiously given the uncertainties associated with the MLS retrievals. Read et al. (2001) showed that the global-averaged accuracy of RH*i* from the MLS retrievals are 22% and 23% at 147 hPa and 215 hPa, respectively.

4.1.2 Effects on cloud fields

Since heterogeneous freezing requires lower RH*i*, we expect that adding heterogeneous IN will lead to cloud fraction increases, which is indeed what we find in the model (Table 2). Total cloud fraction increases from 66.4% in the HOM case to 67.3% in the HMHT_0.01IN case, and further increases to 68.40% in the HMHT_0.1IN case. Because heterogeneous freezing already dominates in the HMHT_0.1IN case, further increases in the number of heterogeneous IN (as in HMHT_1IN) has little or no effect on cloud fraction.

Heterogeneous IN can significantly affect the simulated ice crystal number concentration, as shown in Table 4 and Fig. 10. Figure 10 shows the annual average latitude-pressure cross sections of in-cloud ice crystal number concentration in all cases where the competition between homogeneous freezing and heterogeneous freezing is allowed. The results show that in an environment dominated by homogeneous freezing, the addition of heterogeneous IN decreases the ice crystal number concentration. In both the HOM case and the HMHT_0.01IN case homogeneous freezing dominates,

ACPD
9, 16607–16682, 2009

as seen in the PDF of RH*i* (Fig. 6). Therefore we expect a decrease in ice crystal number concentrations as IN are added. There is a 27% decrease in column-integrated ice crystal number concentration from the HOM case (0.022×10^{10} m^{-2}) to the HMHT_0.01IN case (0.016×10^{10} m^{-2}) and a 47% decrease from the HMHT_0.01IN case (0.016×10^{10} m^{-2}) to the HMHT_0.1IN case (0.0085×10^{10} m^{-2}) (Table 2). Regionally, when 1% of the BC and dust particles are added as heterogeneous IN to the HOM case (compare Fig. 10a and Fig. 4a; Table 4), the frequency of homogeneous freezing in the NH decreases and the ice crystal number concentration decreases, which results in a higher ice crystal number concentration in the SH than in the NH for HMHT_0.01IN (also see Table 4). When IN concentrations are increased by a factor of 10 from the HMHT_0.01IN case to the HMHT_0.1IN case (compare Fig. 10a and b), the frequency of homogeneous freezing decreases significantly everywhere and heterogeneous freezing dominates (Fig. 6). This results in a higher ice crystal number concentration in the NH than in the SH in HMHT_0.1IN (Fig. 10b and Table 4) because the heterogeneous IN concentration is higher in the NH (Fig. 9).

When the environment is dominated by heterogeneous freezing, adding heterogeneous IN increases ice crystal number concentrations. There is a significant increase in ice crystal number concentration in the HMHT_1IN case compared with that in the HMHT_0.1IN case because heterogeneous freezing dominates in the HMHT_0.1IN case (Fig. 10b and c; Table 4). The column-integrated ice crystal number concentration is increased by a factor of 5 from 0.0085×10^{10} m^{-2} in HMHT_0.1IN to 0.051×10^{10} m^{-2} in HMHT_1IN (Table 2). Because of the very high IN concentrations in this case (Fig. 8), homogeneous freezing rarely occurs, and ice crystal number concentration is almost completely determined by heterogeneous freezing. Our results show that the background ice freezing mode determines the sign of the change in ice crystal number concentration from the addition of heterogeneous IN, which is consistent with previous studies (e.g., Hendricks et al., 2005; Penner et al., 2009).

When 1% of soot and dust particles are added as heterogeneous IN to the HOM case, ice crystal number concentration decreases with decreasing temperature at

ACPD
9, 16607–16682, 2009

low temperatures (<195 K) (see Fig. 5c), a feature that is consistent with Krämer et al. (2009), although ice crystal number concentrations still increase as they do in the homogeneous case with increasing temperature at higher temperatures. At low temperatures, because of the low vertical velocities and low mesoscale temperature perturbations, heterogeneous IN decrease the frequency of homogeneous freezing significantly, and decrease ice crystal number concentrations, while at higher temperatures (~200 K), heterogeneous IN have much smaller effects because of the relatively higher vertical velocities and mesocale temperature perturbations. When 10% of the BC and dust particles are added as heterogeneous IN (Fig. 5e), the simulated ice crystal number concentration is less dependent on temperature.

Changes in the ice crystal number concentrations from the addition of heterogeneous IN affect ice crystal radii. Larger ice crystal number concentrations lead to smaller ice crystal radii. The HMHT_1IN case has the largest ice crystal number concentration, which leads to the smallest ice crystal radii at the tops of cirrus clouds (34.56 μm in Table 2). One exception is the HMHT_0.1IN case. Although this case leads to the smallest column-integrated ice number concentration, it has a cloud top ice crystal radius of 42.6 μm which is slightly smaller than that in HMHT_0.01IN (43.6 μm). This can be explained by regional differences between HMHT_0.01IN and HMHT_0.1IN. Although on average the HMHT_0.1IN case has smaller ice crystal number concentrations than does HMHT_0.01IN, it has larger ice crystal number concentrations at the highest levels in the tropics and in the NH, which leads to slightly smaller ice crystal radii at the tops of cirrus clouds (compare Fig. 10a and b).

Since ice crystal radius determines the settling velocity of ice crystals, and since gravitational settling is a very important removal mechanism for cirrus clouds in the upper troposphere, changes in ice crystal radii lead to changes in cirrus cloud lifetimes and ice water content in the upper troposphere. One example is shown in Fig. 3. When ice crystal number concentrations decrease from the HOM case to the HMHT_0.01IN case, ice crystal radius increases, which increases the gravitational settling and decreases ice water content in the upper troposphere (compare Fig. 3b and c). The ex-

ACPD
9, 16607–16682, 2009

cessive ice water simulated over the Arctic in HOM is decreased in the HMHT_0.01IN case, which improves the comparison with MLS observations.

The change in ice crystal size also affects liquid clouds by moistening lower levels in the atmosphere (e.g., Wu, 2002; Grabowski, 2000; Sanderson et al., 2008). Simulated liquid water path and low level cloud fraction are always positively correlated with column-integrated ice crystal number concentration in all our simulations (Table 2). For example, when ice crystal number concentration increases from the HMHT_0.1IN case to the HMHT_1IN case, the liquid water path increases by 9% from 75.3 g/m^2 to 82.0 g/m^2. More ice crystals lead to smaller ice crystal radii, which leads to longer cloud lifetimes in the atmosphere. The longer cloud lifetimes lead to more evaporation from ice crystals and more moisture is transported to the lower atmosphere. This increases low level cloud fraction and the liquid water path. Our results here are consistent with those of Wu (2002) and Grabowski (2000). Both of these studies found that a model with low ice crystal fall velocities would produce a warm, cloudy, moist lower troposphere with less precipitation. This change in liquid clouds in the lower troposphere can have important implications for the simulated net cloud forcing as we show below.

4.1.3 Effects on radiative fluxes

As shown above, heterogeneous IN affect both high cirrus clouds and lower level liquid clouds through their effects on ice crystal number concentration. We show below that changes in both high cirrus clouds and lower level liquid clouds determine the effects of heterogeneous IN on the net cloud radiative forcing.

Changes in both the longwave and shortwave cloud forcing closely follow changes in the simulated ice crystal number concentrations (Tables 2 and 3). Larger ice crystal number concentrations lead to smaller ice crystal radii and more ice water content in the upper troposphere, and a larger liquid water path in the lower atmosphere (Sect. 4.1.2). All these changes lead to a larger longwave cloud forcing (warming) and larger shortwave cloud forcing (cooling). The HMHT_0.1IN case simulates the smallest longwave cloud forcing (26.22 W/m^2) and the smallest shortwave cloud forc-

ACPD
9, 16607–16682, 2009

ing (50.65 W/m^2) because it has the lowest ice crystal number concentration. The opposite is true for the HMHT_1IN case, which simulates the largest longwave and shortwave cloud forcing.

The simulated net cloud forcing is more complex. Although both longwave and shortwave cloud forcing are affected by changes in high level cirrus clouds and lower level liquid clouds, changes in high level cirrus clouds have a larger effect on longwave cloud forcing and changes in low level liquid clouds have a larger effect on shortwave cloud forcing (e.g., Chen et al., 2000). So changes in the net cloud forcing depend on whether changes in high cirrus clouds or changes in low level liquid clouds dominate. When column-integrated ice crystal number concentrations decrease by 27% from the HOM case to the HMHT_0.01IN case, the net cloud forcing changes from -24.61 W/m^2 to -24.75 W/m^2 so that a net cooling of 0.14 W/m^2 is simulated, which indicates that the cooling is caused by increases in ice crystal radius and decreases in ice water in high cirrus clouds which dominate the effects on liquid water clouds. But when columned-integrated ice crystal number concentration decreases further by 47% from the HMHT_0.01IN case to the HMHT_0.1IN case, a net warming of 0.32 W/m^2 is simulated, which indicates that the warming is caused by decreases in low level liquid clouds that dominate the effects on cirrus clouds. Compared with the HMHT_0.01IN case, the HMHT_0.1IN case simulates a 1.5% decrease in liquid water path (75.26 vs. 76.44 g/m^2), due to the moistening effects of ice crystals on the lower atmosphere, as discussed in Sect. 4.1.2.

The moistening effect of ice crystal gravitational settling on the lower atmosphere has been recognized for a long time (e.g., Wu, 2002; Grabowski, 2000; Sanderson et al., 2008). Our results suggest that the sign of the change in the net cloud forcing caused by heterogeneous IN is determined not only by the ice freezing mode in the background atmosphere, but also by the change in liquid clouds from this moistening effect. The effects of liquid cloud changes caused by the moistening effect tend to counteract the effects of high level cirrus cloud changes. So the change in the net cloud forcing is relatively less sensitive to changes in ice crystal number concentrations caused by

ACPD
9, 16607–16682, 2009

heterogeneous IN (or even by changes in mesoscale dynamics as will be discussed in next section). The net cloud forcing in the four simulations discussed here ranges from $-24.30\,W/m^2$ to $-24.75\,W/m^2$, with a maximum change of $0.45\,W/m^2$, which is small considering the fact that a two order of magnitude change in IN concentrations was imposed.

Although the net change in cloud forcing is relatively small and the sign of the cloud forcing change depends on the competition between changes in high cirrus clouds and changes in low level liquid clouds, the change in the net radiative fluxes (FNT) at the TOA is large, with a maximum change of $2.2\,W/m^2$ between the four cases discussed here. This change closely follows the change in ice crystal number concentration, as shown in Table 2, i.e., higher ice crystal number concentrations lead to more warming at the TOA. The large changes in the net radiative flux at the TOA mainly comes from the change in clear sky longwave radiation due to changes in water vapor in the atmosphere, especially in the upper troposphere. Higher ice crystals lead to smaller ice crystal radius, which leads to longer cloud lifetimes and therefore more water vapor in the upper troposphere. Also, heating from more ice crystals warms the upper troposphere and leads to higher temperatures and to more water vapor in both the upper troposphere and stratosphere. The greenhouse effect of water vapor depends more on the relative change and less on the absolute change in water vapor (Raval and Ramanathan, 1989). Although the absolute change in the water vapor concentration in the upper troposphere is small between the different cases, the relative change can be large. For example, the integrated water vapor mass from 100 hPa to 300 hPa decreases by 12% from the HOM case to the HMHT_0.1IN case, which contributes the most to the clear sky longwave cooling of $1\,W/m^2$. This overrides the warming in the net cloud forcing and leads to a net cooling of $0.92\,W/m^2$ at the TOA. Stratospheric water vapor also decreases significantly from the HOM case to the HMHT_0.1IN case (~35%), but results from a 1-D radiative transfer model calculation with a typical tropical profile in winter from the GCM show that the change in stratospheric water vapor has little effect on the clear sky TOA longwave radiative flux (i.e., removal of 35% of

ACPD
9, 16607–16682, 2009

the stratospheric water vapor had a similar TOA longwave flux as that with the full profile) though the change in stratospheric water vapor can have important effects on the clear sky radiative fluxes at the tropopause, which is consistent with Forster and Shine (2002). The 1-D radiative transfer calculation showed that a 35% decrease in the stratospheric water vapor leads to a cooling of 0.70 W/m^2 at the tropopause.

In summary, changes in ice crystal number concentrations, caused by either homogeneous freezing or heterogeneous freezing, change the TOA radiative fluxes through three effects: net changes dominated by the change in the longwave cloud radiation caused by changes in high level cirrus clouds, net changes dominated by the changes in shortwave cloud radiation caused by changes in low level liquid clouds, and changes in the clear sky long wave radiation caused by changes in water vapor in the upper troposphere. The first and the third effects act in the same direction, but the second effect acts in the opposite direction. Due to the cancellation of the first and second effects, the net change in cloud forcing is less sensitive to changes in ice crystal number concentration and the net flux change at the TOA is mainly controlled by changes in the clear sky long wave radiation in this study.

4.2 Effects of mesoscale temperature perturbations

The effects of mesoscale temperature perturbations on simulated cirrus cloud properties were examined in two additional sensitivity tests (HMHT_0.75dT and HMHT_1.25dT). These two cases have the same IN concentration as in the HMHT_0.01IN case, but here the temperature perturbation decreases or increases by 25%.

A 25% higher temperature perturbation in the HMHT_1.25dT case leads to a 25% higher cooling rate and vertical velocity since these latter two parameters are proportional to the temperature perturbation in our treatment (see Eq. (4) in Sect. 2.2). Higher cooling rates and vertical velocities limit the influence of heterogeneous IN, and lead to more homogeneous freezing, as seen in the simulated PDF of RHi in the NH middle latitudes at both 100–200 hPa and 200–300 hPa (Fig. 6), and therefore lead to higher

ACPD
9, 16607–16682, 2009

frequencies of RHi>150% than in the HMHT_0.01IN case. The opposite is true when the temperature perturbation is decreased by 25% in the HMHT_0.75dT case, which increases the influence of heterogeneous IN and leads to less homogeneous freezing (Fig. 6).

Simulated ice crystal number concentrations in HMHT_1.25dT are higher than in HMHT_0.01IN (compare Fig. 10a and e; Table 4). The competition between heterogeneous and homogeneous freezing coupled with the higher cooling rate leads to higher ice crystal numbers generated from homogeneous freezing. The column-integrated ice crystal number concentration increases by 50% from $0.016\times10^{10}\,m^{-2}$ in the HMHT_0.01IN case to $0.024\times10^{10}\,m^{-2}$ in the HMHT_1.25dT case. The opposite is true for the HMHT_0.75dT case (compare Fig. 10a and d; Table 4). Homogeneous freezing occurs less often so that the simulated column integrated ice crystal number concentration decreases by 50% from $0.016\times10^{10}\,m^{-2}$ in the HMHT_0.01IN case to $0.0089\times10^{10}\,m^{-2}$ in the HMHT_0.75dT case.

The change in radiative fluxes depends on changes in ice crystal number concentration, as discussed in Sect. 4.1.3. A net warming of $0.46\,W/m^2$ in the cloud forcing is simulated in going from the HMHT_0.75dT case to the HMHT_1.25dT case, but this only contributes about one third to the increase in the simulated net TOA flux difference, which is $1.27\,W/m^2$. The remaining two thirds of the increase comes from the greenhouse effect of increased water vapor in the upper troposphere from the decreased crystal size, which results from an increase in the ice crystal number concentration.

The magnitude of the changes in the net cloud forcing and net TOA fluxes from different mesoscale temperature perturbations are comparable to those simulated from different heterogeneous IN concentrations (Sect. 4.1.3). For example, a 25% decrease in the temperature perturbation from the HMHT_0.01IN case to the HMHT_0.75dT case leads to a net cooling of $0.22\,W/m^2$ in the cloud forcing and a net TOA cooling of $0.54\,W/m^2$, while a factor of 10 increase in the heterogeneous IN concentration from the HMHT_0.01IN case to the HMHT_0.1IN case leads to a net warming of $0.32\,W/m^2$ in the cloud forcing and a net TOA cooling of $0.43\,W/m^2$. This points to the importance

ACPD
9, 16607–16682, 2009

of mesoscale dynamics and subgrid scale variations in studying aerosol indirect effects on cirrus clouds (Haag and Kärcher, 2004; Penner et al., 2009).

5 Conclusions and discussion

We implemented the statistical cirrus cloud scheme presented in KB08 in the NCAR CAM3 atmospheric circulation model component of the coupled IMPACT/CAM model. This cirrus cloud scheme has an assumed subgrid scale temperature variation in the clear sky and a variation of in-cloud water concentration in the cloudy sky, and has a consistent treatment for the nucleation of ice crystals and cloud fraction. The coupled model with the new cirrus cloud scheme is evaluated by comparing model results with observations, and the effects of heterogeneous IN and mesoscale temperature perturbations are examined using sensitivity tests.

The simulated model fields, including the liquid water path, ice water path, shortwave cloud forcing, longwave cloud forcing, cloud fraction, and precipitation are in reasonable agreement with observations. The direct conversion from liquid water to ice water in mixed-phase clouds decreases the liquid water path significantly compared to that in the standard CAM3, and the resulting liquid water path in different cases ranges from 75 to 82 g/m^2, which is in better agreement with observations than that simulated by the standard CAM3. The new cirrus cloud scheme simulates significantly smaller high cloud fractions than in LIU07, where cloud fraction was diagnosed as in the standard CAM3 based on relative humidity. The simulated total cloud fraction ranges from 66.4% to 68.5% in all cases, and agrees well with observations. The simulated ice water content in the homogeneous freezing only case (HOM) broadly captures the spatial and zonal distribution of ice water content in the upper troposphere in the MLS data, but it underestimates ice water content in the tropics by a factor of 2 to 4. The ice water content simulated in this case also spreads more toward the poles than in the MLS data, a feature that is improved when 1% of the BC and dust particles are added as heterogeneous IN.

ACPD
9, 16607–16682, 2009

When only homogeneous freezing is included in the model, the simulated PDF of RH*i* outside of cirrus clouds has an exponential decay from 100% RH*i* to 150% RH*i* which agrees with MOZAIC field data. A faster decay is simulated beyond 150% due to homogeneous freezing. Including heterogeneous IN changes the PDF of the RH*i* significantly. When 1% of the BC and dust particles act as heterogeneous IN with a low threshold freezing humidity of about 120–130% RH*i*, the frequency of occurrence of very high RH*i* at 200–300 hPa in the NH middle latitudes decreases, but there is little effect in the SH and tropics and at high altitudes. The simulated hemispheric contrast in the PDF of the RH*i* in this case is consistent with that observed in the INCA field campaign (Haag et al., 2003). When heterogeneous IN concentrations are increased by a factor of 10, the frequency of high RH*i* decreases significantly in both hemispheres, which is not supported by the MOZAIC data.

The simulated frequency of supersaturation at 139 hPa and 192 hPa agrees well with satellite observations in terms of its spatial distribution, but the model overestimates the magnitude of the supersaturation frequency when only homogeneous freezing is included, especially at 192 hPa. Including heterogeneous IN in the model decreases the supersaturation frequency and improves the comparison with satellite observations at 192 hPa, which supports the notion that heterogeneous freezing plays a role in ice freezing.

Simulated ice crystal number concentrations from the prognostic ice crystal equation are smaller by a factor of 2–5 than those immediately after initial ice nucleation, which points to the importance of having a prognostic ice crystal equation in the model. Ice crystal number concentrations immediately after the initial ice nucleation from homogeneous freezing are comparable with those from the INCA observations, which represent young clouds that have not undergone aging.

Heterogeneous IN affect cirrus cloud properties significantly, and their exact effects depend on the background freezing modes. In an atmosphere dominated by homogeneous freezing, as in the HOM and HMHT_0.01IN cases, adding heterogeneous IN decreases ice crystal concentrations and increases cirrus cloud fraction. This explains the

ACPD
9, 16607–16682, 2009

27% decrease in simulated column-integrated ice crystal concentration from the HOM case to the HMTH_0.01IN case, as well as the 47% decrease from the HMTH_0.01IN case to the HMHT_0.1IN case. But in an atmosphere dominated by heterogeneous freezing, as in the HMHT_0.1IN case, adding heterogeneous IN increases the ice crystal number concentration and has little effect on the cirrus cloud fraction. This explains the factor of 5 increase in simulated column-integrated ice crystal number concentration in the HMHT_1IN case compared with that in the HMHT_0.1IN case.

Changes in mesoscale temperature perturbations also change ice crystal number concentrations significantly. Large temperature perturbations produce higher cooling rates and therefore more homogeneous freezing and higher ice crystal number concentrations, while smaller temperature perturbations produce lower cooling rates and therefore less homogeneous freezing and smaller ice crystal number concentrations. Column-integrated ice crystal number concentrations increase by 50% from the HMHT_0.01IN case to the HMHT_1.25dT case when the mesoscale temperature perturbation is increased by 25%, while it decreases by 50% from the HMHT_0.01IN case to the HMHT_0.75dT case when the mesoscale temperature perturbation decreases by 25%. Changes in ice crystal number concentrations from a 25% change in the temperature perturbation have a magnitude that is similar to those caused by a factor of 10 change in the heterogeneous IN concentrations. This reinforces the importance of having a better representation of mesoscale dynamic forcing in the treatment of cirrus clouds and in studies of the indirect effects of aerosols on cirrus clouds (Haag and Kärcher, 2004).

Changes in the ice crystal number concentration, caused by either heterogeneous IN or by mesoscale temperature perturbations, affect ice crystal radius, ice water content, low level liquid clouds, and water vapor in the atmosphere. More ice crystals lead to smaller ice crystal radii and smaller ice settling velocities. This leads to not only more ice water and more water vapor in the upper troposphere, but also to a more cloudy and more moist lower troposphere. This moistening effect on low level clouds is ubiquitously seen across all simulations, as the liquid water path and low level cloud fraction are

ACPD
9, 16607–16682, 2009

always positively correlated with the simulated ice crystal number concentration (i.e., smaller ice crystal number concentration leads to smaller low level cloud fraction and to smaller liquid water path).

Changes in the net radiative fluxes at the TOA are determined by the following three changes: 1) the change in the net radiation caused by the change in high level cirrus clouds; 2) the change in the net radiation caused by the change in low level liquid clouds; and 3) the change in the clear sky longwave radiation caused by the change in water vapor in the upper troposphere. The first and the third effects act in the same direction, but the second effect acts in the opposite direction. Due to the cancellation of the first and second effects, the net change in cloud forcing is less sensitive to changes in ice crystal number concentration (a maximum change of 0.67 W/m^2 in the net cloud forcing is simulated across all cases in this study) while the sign of the change in the cloud forcing depends on which of these two effects dominates. Our results show that either of these two effects can dominate. A net cooling of 0.14 W/m^2 is simulated in going from the HOM case to the HMHT_0.01IN case, which indicates that the first effect dominates, while a net warming of 0.32 W/m^2 is simulated in going from the HMHT_0.01IN case to the HMTH_0.1IN case, which indicates that the second effect dominates, though ice crystal number concentrations increase in both scenarios. The reason for this difference is not immediately clear, but it may depend on the differences in the simulated ice crystal number concentration changes with altitude. For example, ice crystal number concentrations at the uppermost level in the tropics increase but they decrease at most of the other levels in the second scenario, while ice crystal number concentrations decrease at all levels in the first scenario (see Fig. 4a and 10a–b).

Because the net change in cloud forcing is less sensitive to changes in ice crystal number concentration due to the competition between the first and second effects, the net flux changes at the TOA are mainly controlled by the change in upper tropospheric water vapor which closely follows the change in the ice crystal number concentration (more ice crystals lead to more warming). A maximum change of 2.35 W/m^2 is simulated across all the cases in this study, where the net cloud forcing change contributes

ACPD
9, 16607–16682, 2009

0.65 W/m^2 to this change, and the remaining 1.67 W/m^2 is caused by the changes in the greenhouse effects of water vapor. The large change in the greenhouse effect of water vapor may point to a problem in studies of aerosol indirect effects on cirrus clouds that only examine the change in cloud forcing.

Our study shows that ice crystal gravitational settling plays a central role in determining the aerosol indirect effects on clouds. This points to the urgent need to improve the representation of gravitational settling in models, as has been highlighted in several recent studies (e.g., Sanderson et al., 2008; Mitchell et al., 2008).

Appendix A Equations used in the cirrus cloud scheme

The key equations used in the cirrus cloud scheme of KB08 are listed in this Appendix, and readers are referred to KB08 for details.

The PDF of clear sky temperature is approximated by a constrained normal distribution with mean temperature (T_0) and standard deviation δT:

$$\frac{dP_T}{dT} = \frac{1}{N_T}\frac{1}{\delta T}\frac{1}{\sqrt{2\pi}}\exp\{\frac{-(T-T_0)^2}{2\delta T^2}\}, \quad \text{(A1)}$$

where $dP_T/dT=0$ outside of $T_0 \pm 3\delta T$ and N_T is a normalization factor accounting for the finite limits over which Eq. (A1) is defined.

By using the saturation vapor pressure over pure hexagonal ice which is calculated based on Murphy and Koop (2005), the PDF of clear sky temperature is then transformed into the PDF of clear sky saturation ratio (S):

$$\frac{dP_s}{dS} = \frac{1}{N_S}\frac{1}{\sigma_S\sqrt{2\pi}}\frac{1}{S\ln^2(S/\alpha)} \times \exp[-\beta_S\{\frac{1}{\ln(S/\alpha)} - \frac{1}{\ln(S_0/\alpha)}\}^2], \quad \text{(A2)}$$

where $\beta_s=1/(2\sigma_S^2)$, $\sigma_S=\delta T/\theta$, $\theta=6132.9$ K, $\alpha=p_v/\phi$, $\phi=3.4452\times10^{10}$ hPa, and p_v is the water vapor partial pressure. S_0 is the mean clear sky saturation ratio and N_S is a

ACPD
9, 16607–16682, 2009

normalization factor, which is calculated as

$$N_S = \frac{1}{2}(\mathrm{erf}[\sqrt{\beta_S}\{\frac{1}{\ln(S_0/\alpha)} - \frac{1}{\ln(S_{3+}/\alpha)}\}] - \mathrm{erf}[\sqrt{\beta_S}\{\frac{1}{\ln(S_0/\alpha)} - \frac{1}{\ln(S_{3-}/\alpha)}\}], \quad \text{(A3)}$$

where S_{3+} and S_{3-} are the upper and lower bounds of S at which dP_s/dS is defined (i.e., dP_s/dS=0 outside of [S_{3-}, S_{3+}]) and $S_{3\pm}$ is calculated as:

$$S_{3\pm} \approx S_0 \exp(\frac{\pm 3\delta T\theta}{T_0^2}). \quad \text{(A4)}$$

Here, erf(x) is the error function and is defined as:

$$\mathrm{erf}(x) = (2/\sqrt{\pi})\int_0^x \exp(-t^2)dt. \quad \text{(A5)}$$

The in-cloud vapor deposition/evaporation is calculated as

$$(\frac{\partial q_{vc}}{\partial t})_{\mathrm{dep}} = -4\pi D N_i r \beta C \phi (q_{vc} - q_{\mathrm{sat}}) = -\frac{q_{vc} - q_{\mathrm{sat}}}{\tau_s}, \quad \text{(A6)}$$

where N_i is the in-cloud ice crystal number concentration, r is the volume mean radius, D is the diffusion coefficient of water molecules in air, C and ϕ are the ice crystal capacitance and ventilation factors, β accounts for gas kinetic corrections, and τ_s is the instantaneous relaxation time-scale given by:

$$\tau_s = \frac{1}{4\pi D N_i r \beta C \phi}. \quad \text{(A7)}$$

C, ϕ, and β are set equal to unity in this study. Integrating Eq. (A5) over a time step τ yields the vapor deposition formula given in Eq. (8).

The PDF of the in-cloud ice water content (q_i) (dP_{q_i}/dq_i) is represented by the following formula:

$$q_i \frac{dP_{q_i}}{dq_i} = \frac{2}{\sqrt{\pi}}(\frac{q_i}{q_{i0}})\exp\{-(\frac{q_i}{q_{i0}})^2\}, \quad q_{i0} = \sqrt{\pi}\bar{q}_i, \quad \text{(A8)}$$

ACPD
9, 16607–16682, 2009

where $\bar{q}_i$ is the mean ice water content. This PDF of in-cloud ice water content was shown to be a good approximation of the cirrus ice water content observed over Punta Arenas, Chile (Ström et al., 2003; KB08). The PDF of in-cloud water vapor is assumed to be a homogeneous distribution in the form of a delta function. Therefore, the PDF of the total water mass mixing ratio in cloudy areas (q_{totc}) is:

$$\frac{dP_{q_{\text{totc}}}}{dq_{\text{totc}}} = \frac{2}{\sqrt{\pi}}\frac{1}{q_0}\exp\{-(\frac{q_{\text{totc}} - q_{vc}}{q_0})^2\}, \quad q_0 = \sqrt{\pi}\frac{q_i}{a}, \tag{A9}$$

where q_i/a denotes the simulated in-cloud ice mass mixing ratio and $q_{\text{totc}} \geq q_{vc}$. This PDF for the total water mixing ratio is used to calculate changes in cloud fraction and ice water content by Eqs. (9) and (10), respectively.

Appendix B A two-moment treatment of cloud microphysics for warm and mixed-phase clouds

In addition to the new cirrus cloud scheme described in Sect. 2.2, a prognostic cloud droplet number concentration (n_l) equation for liquid clouds is added in the version of CAM3 used in this study compared with the version used in LIU07. Together with the prognostic liquid water mass (q_l), ice water mass (q_i), and ice crystal number concentration (n_i), the complete set of equations for the two-moment treatment of cloud microphysics for liquid clouds and mixed-phase clouds are:

$$\frac{\partial q_l}{\partial t} = A(q_l) + \text{DTR}(q_l) + Q_{\text{cond}} - Q_{\text{liq2pr}} - Q_{\text{liq2ice}}, \tag{B1}$$

$$\frac{\partial q_i}{\partial t} = A(q_i) + \text{DTR}(q_i) + Q_{\text{liq2ice}} + Q_{\text{vap2ice}} - Q_{\text{ice2pr}}, \tag{B2}$$

$$\frac{\partial n_l}{\partial t} = A(n_l) + \text{DTR}(n_l) + N_{\text{nucl}} - N_{\text{self}} - N_{\text{liq2pr}} - N_{\text{evapl}} - N_{\text{liq2ice}} \tag{B3}$$

ACPD
9, 16607–16682, 2009

$$\frac{\partial n_i}{\partial t} = A(n_i) + \mathrm{DTR}(n_i) + N_{\mathrm{nuci}} + N_{\mathrm{frz}} + N_{\mathrm{sec}} - N_{\mathrm{ice2pr}} - N_{\mathrm{evapi}}, \quad \text{(B4)}$$

where the A operator on the left side of Eqs. (B1–B4) represents the advective, turbulent, and convective transports, as well as the gravitational settling, and the DTR operator represents the detrained cloud liquid and ice from both deep and shallow convection.

Q_{cond} represents the net condensation rate for liquid clouds in warm and mixed-phase clouds as diagnosed by the fractional cloud closure scheme of Zhang et al. (2003), and acts to remove any supersaturation with respect to water (LIU07). Q_{liq2pr} and Q_{ice2pr} are the loss rates of cloud liquid mass and ice mass from the conversion of cloud condensate into precipitation, respectively. They include the auto-conversion of liquid water to rain, the collection of cloud water by rain from above, the auto-conversion of ice to snow, the collection of ice by snow, and the collection of liquid by snow (Rasch and Kristjánsson, 1998). Q_{vap2ice} represents the deposition on ice crystals from water vapor (LIU07). Q_{liq2ice} represents the growth of ice water at the expense of liquid water due to the Bergeron-Findeisen process in mixed-phase clouds, and is calculated based on Rotstayn et al. (2000). The in-cloud saturation vapor pressure used to calculate ice supersaturation in mixed-phase clouds is the saturation vapor pressure weighted by the proportions of ice and liquid water mass. This direct conversion from liquid to ice was not allowed in LIU07 who assumed a conversion from water vapor to ice which resulted in a smaller conversion rate of liquid to ice in mixed-phase clouds. This direct conversion was used in simulating observed clouds in the Mixed-Phase Arctic Cloud Experiment (M-PACE) in a single column model (Liu et al., 2007b) and in a short-range weather forecasting approach (Xie et al., 2008).

Detrained cloud mass from convection is assumed to be in the liquid phase for clouds warmer than -35°C, and is assumed to be in the ice phase for cirrus clouds. The conversion of this detrained condensate from liquid phase into the ice phase in the mixed-phase clouds is completed through the Bergeron-Findeisen process. Detrained cloud droplet number concentration and ice crystal number concentration are calcu-

ACPD
9, 16607–16682, 2009

lated from detrained cloud liquid and ice mass by assuming a spherical particle with constant volume-mean radius for both cloud droplets and ice crystals. These volume-mean radii for liquid droplets and ice crystals are calculated from the effective radius used in the standard CAM3 (Boville et al., 2006), following the treatment in LIU07 for ice crystals.

Microphysical terms for the cloud droplet number concentration (n_l) include the droplet source from activation (N_{nucl}), and droplet sinks from precipitation (N_{liq2pr}), evaporation (N_{evapl}), self-collection (N_{self}), and freezing (N_{liq2ice}). The loss rate of cloud droplet number concentration from precipitation is assumed to be proportional to the loss rate of liquid water mass from precipitation, and is calculated as

$$N_{\text{liq2pr}} = \frac{Q_{\text{liq2pr}}}{q_l} n_l. \tag{B5}$$

The same assumption is applied to the loss rate of cloud droplet number concentration from evaporation. Only the net evaporation rate of cloud liquid mass (Q_{cond}) is diagnosed in CAM3, using the scheme of Zhang et al. (2003). Here we assume that the evaporation of cloud droplets only occurs when there is net evaporation of cloud liquid mass, and is calculated as:

$$N_{\text{evapl}} = \frac{-\min(0, Q_{\text{cond}})}{q_l} n_l. \tag{B6}$$

The depletion of cloud droplets from the freezing process (N_{liq2ice}) includes the initial freezing of cloud droplets into ice crystals from contact freezing (N_{frz}), and the depletion of cloud droplets from the Bergeron-Findeisen process. The fraction of cloud liquid droplet number concentration depleted due to the Bergeron-Findeisen process is assumed to be half of that of the cloud liquid mass depleted due to the same process (Q_{liq2ice}), except when the cloud liquid mass is completely depleted, and then all cloud droplets are depleted. Thus, we assume that part of the cloud mass that is depleted from the Bergeron-Findeisen process comes from the shrinking of cloud droplets.

ACPD
9, 16607–16682, 2009

The droplet activation term (N_{nucl}) follows the treatment of Lohmann et al. (1999). New droplets are assumed to form only when the number concentration of cloud droplets that would be activated exceeds the number concentration of preexisting cloud droplets and when net condensation occurs:

$$N_{nucl} = \max[\frac{1}{\Delta t}(N_{ac} f - n_{old}), 0], \quad \text{when} \quad Q_{cond} > 0, \tag{B7}$$

where N_{ac} is the number concentration of cloud droplets activated from aerosol particles, and n_{old} is the grid-mean cloud droplet number concentration predicted by Eq. (B3) at the previous time step. N_{ac} is calculated from aerosol fields using a parameterization based on Köhler theory (Abdul-Razzak and Ghan, 2000, 2002). This parameterization combines the treatment of multiple aerosol types and a sectional representation of size to deal with arbitrary aerosol mixing states and arbitrary aerosol size distributions. Five categories of aerosols are externally mixed: sulfate, biomass burning OM/BC, fossil fuel OM/BC, sea salt, and dust. The bulk hygroscopicity parameter for each category of aerosol is the volume-weighted average of the parameters for each component taken from Ghan et al. (2001) (also see Table 2 in Wang and Penner, 2009). The size distributions of the five types of aerosols are prescribed as in Table B1. The vertical velocity (w) used in calculating N_{ac} is calculated from $w = \bar{w} + c \times \sigma_w$, where $\bar{w}$ is the large-scale vertical velocity, σ_w is the subgrid variance of the vertical velocity diagnosed from the eddy diffusivity and the mixing length, and c is a coefficient that depends on σ_w(Wang and Penner, 2009).

The self-collection of cloud droplets follows the treatment of Beheng (1994) and is parameterized as

$$N_{self} = 1.29 \times 10^{10} \times b(\rho \frac{q_l}{f})^2, \tag{B8}$$

where ρ is the air density (kg/m^3).

The source and sink terms of ice crystal number concentration include deposition/condensation freezing (N_{nuci}), contact freezing of cloud droplets from dust particles

ACPD
9, 16607–16682, 2009

(N_{frz}), the secondary ice production by ice splintering between −3 and −8°C (N_{sec}), the loss from precipitation (N_{ice2pr}), and the loss from sublimation of ice crystal particles (N_{sublim}). These source and sink terms are described in LIU07, with modifications as follows. In LIU07, ice particles are assumed to evaporate completely only when cloud dissipates as the cloud fraction (a) decreases. In addition to the evaporation assumed in LIU07, we assumed in this study that ice crystal particles that are advected into the clear sky part of a grid box also evaporate, which is consistent with the treatment of cloud condensate from the scheme of Zhang et al. (2003).

The effective radii of ice crystals is parameterized from the ice crystal number concentration, ice water content, and temperature as described in Chen (2006) and LIU07. Cloud droplet effective radius (r_{el}) is calculated from the volume-mean cloud droplet radius (r_{vl}) based on the parameterization of Rotstayn and Liu (2003), which takes account of the change in the dispersion of the cloud droplet size distribution caused by the change in the cloud droplet number concentration. r_{el} is calculated as:

$$r_{el} = \beta r_{vl}, \tag{B9}$$

where β is the droplet size spectral shape factor and is approximated as:

$$\beta = \frac{(1+2\varepsilon^2)^{2/3}}{(1+\varepsilon^2)^{1/3}}, \tag{B10}$$

where ε is the relative dispersion of the size distribution of cloud droplets and is approximated as:

$$\varepsilon = 1 - 0.7\exp(-\alpha N_l), \tag{B11}$$

where N_l is the in-cloud droplet number concentration, and α is a coefficient. An α of 0.003 is used in this study, which represents the middle curve that fits the observed ε and N_l in Fig. 1 of Rotstayn and Liu (2003).

Acknowledgements. We thank Xiaohong Liu in Pacific Northwest National Laboratory for many helpful discussions regarding the cirrus cloud treatment in LIU07 and for Yuxing Yun at the

University of Michigan for the discussions regarding the ice nucleation treatment in mixed-phase clouds. This work was funded in part by NSF projects ATM 0333016 and ATM 0609836. Computer time was provided by the NCAR CISL facility.

References

Abbatt, J. P. D., Benz, S., Cziczo, D. J., Kanji, Z., Lohmann, U., and Möhler, O.: Solid ammonium sulfate aerosols as ice nuclei: A pathway for cirrus cloud formation, Science, 313, 1770–1773, doi:10.1126/science.1129726, 2006.

Abdul-Razzak, H. and Ghan, S. J.: A parameterization of aerosol activation 2. Multiple aerosol types, J. Geophys. Res., 105, 6837–6844, 2000.

Abdul-Razzak, H. and Ghan, S. J.: A parameterization of aerosol activation 3. Sectional representation, J. Geophys. Res., 107, 4026, doi:10.1029/2001JD000483, 2002.

Andres, R. J. and Kasgnoc, A. D.: A time-averaged inventory of subaerial volcanic sulfur emissions, J. Geophys. Res., 103, 25251–25261, 1998.

Bacmeister, J. T., Eckermann, S. D., Tsias, A., Carslaw, K. S., and Peter, T.: Mesoscale temperature fluctuations induced by a spectrum of gravity waves: A comparison of parameterizations and their impact on stratospheric microphysics, J. Atmos. Sci., 56, 1913–1924, 1999.

Beheng, K. D.: A parameterization of warm cloud microphysical conversion processes, Atmos. Res., 33, 193–206, 1994.

Boville, B. A., Rasch, P. J., Hack, J. J., and McCaa, J. R.: Representation of clouds and precipitation processes in the Community Atmosphere Model version 3 (CAM3), J. Climate, 19, 2184–2198, 2006.

Burkhardt, U., Kärcher, B., Ponater, M., Gierens, K., and Gettelman, A.: Contrail cirrus supporting areas in model and observations, Geophys. Res. Lett., 35, L16808, doi:10.1029/2008gl034056, 2008.

Cantrell, W. and Heymsfield, A.: Production of ice in tropospheric clouds - A review, B. Am. Meteor. Soc., 86, 795–807, 2005.

Chen, Y. L., Kreidenweis, S. M., McInnes, L. M., Rogers, D. C., and DeMott, P. J.: Single particle analyses of ice nucleating aerosols in the upper troposphere and lower stratosphere, Geophys. Res. Lett., 25, 1391–1394, 1998.

Chen, T., Rossow, W. B., and Zhang, Y. C.: Radiative effects of cloud-type variations, J. Climate, 13, 264–286, 2000.
Chen, Y.: Aerosol indirect effects on clouds and global climate, PhD, Department of Atmospheric, Oceanic, and Space Sciences, University of Michigan, Ann Arbor, MI, 218 pp., 2006.
Collins, W. D.: Parameterization of generalized cloud overlap for radiative calculations in general circulation models, J. Atmos. Sci., 58, 3224–3242, 2001.
Collins, W. D., Bitz, C. M., Blackmon, M. L., Bonan, G. B., Bretherton, C. S., Carton, J. A., Chang, P., Doney, S. C., Hack, J. J., Henderson, T. B., Kiehl, J. T., Large, W. G., McKenna, D. S., Santer, B. D., and Smith, R. D.: The Community Climate System Model version 3 (CCSM3), J. Climate, 19, 2122–2143, 2006.
Collins, W. D., Rasch, P. J., Boville, B. A., Hack, J. J., McCaa, J. R., Williamson, D. L., Briegleb, B. P., Bitz, C. M., Lin, S. J., and Zhang, M. H.: The formulation and atmospheric simulation of the Community Atmosphere Model version 3 (CAM3), J. Climate, 19, 2144–2161, 2006.
Cziczo, D. J., Murphy, D. M., Hudson, P. K., and Thomson, D. S.: Single particle measurements of the chemical composition of cirrus ice residue during CRYSTAL-FACE, J. Geophys. Res., 109, D04201, doi:10.1029/2003JD004032, 2004.
Cziczo, D. J., Stetzer, O., Worringen, A., Ebert, M., Weinbruch, S., Kamphus, M., Gallavardin, S. J., Curtius, J., Borrmann, S., Froyd, K. D., Mertes, S., Möhler, O., and Lohmann, U: Inadvertent climate modification due to anthropogenic lead, Nature Geoscience, 2, 333–336, doi:10.1038/NGEO499, 2009.
de Reus, M., Dentener, F., Thomas, A., Borrmann, S., Ström, J., and Lelieveld, J.: Airborne observations of dust aerosol over the North Atlantic Ocean during ACE 2: Indications for heterogeneous ozone destruction, J. Geophys. Res., 105, 15263–15275, 2000.
DeMott, P. J., Rogers, D. C., and Kreidenweis, S. M.: The susceptibility of ice formation in upper tropospheric clouds to insoluble aerosol components, J. Geophys. Res., 102, 19575–19584, 1997.
DeMott, P. J., Sassen, K., Poellot, M. R., Baumgardner, D., Rogers, D. C., Brooks, S. D., Prenni, A. J., and Kreidenweis, S. M.: African dust aerosols as atmospheric ice nuclei, Geophys. Res. Lett., 30, 1732, doi:10.1029/2003GL017410, 2003.
Eyers, C. J., Norman, P., Middel, J., Plohr, M., Michot, S., Atkinson, K., and Christou, R. A.: AERO2k Global Aviation Emissions Inventories for 2002 and 2025, QinetiQ/-4/01113, online available at: http://www.cate.mmu.ac.uk/reports_aero2k.asp?chg=projects&chg2=2⟩

ACPD
9, 16607–16682, 2009

http://www.cate.mmu.ac.uk/reports_aero2k.asp?chg=projects&chg2=2, 2004.
Ferraro, R. R., Weng, F. Z., Grody, N. C., and Basist, A.: An eight-year (1987-1994) time series of rainfall, clouds, water vapor, snow cover, and sea ice derived from SSM/I measurements, B. Am. Meteor. Soc., 77, 891–905, 1996.
Forster, P. M. D. and Shine, K. P.: Assessing the climate impact of trends in stratospheric water vapor, Geophys. Res. Lett., 29, 1086, doi:10.1029/2001gl013909, 2002.
Fritts, D. C. and Alexander, M. J.: Gravity wave dynamics and effects in the middle atmosphere, Rev. Geophys., 41, 1003, doi:10.1029/2001rg000106, 2003.
Gallagher, M. W., Connolly, P. J., Whiteway, J., Figueras-Nieto, D., Flynn, M., Choularton, T. W., Bower, K. N., Cook, C., Busen, R., and Hacker, J.: An overview of the microphysical structure of cirrus clouds observed during EMERALD-1, Q. J. Roy. Meteorol. Soc., 131, 1143–1169, doi:10.1256/Qj.03.138, 2005.
Gary, B. L.: Mesoscale temperature fluctuations in the stratosphere, Atmos. Chem. Phys., 6, 4577–4589, 2006, http://www.atmos-chem-phys.net/6/4577/2006/.
Gary, B. L.: Mesoscale temperature fluctuations in the Southern Hemisphere stratosphere, Atmos. Chem. Phys., 8, 4677–4681, 2008, http://www.atmos-chem-phys.net/8/4677/2008/.
Gayet, J. F., Auriol, F., Minikin, A., Ström, J., Seifert, M., Krejci, R., Petzold, A., Febvre, G., and Schumann, U.: Quantitative measurement of the microphysical and optical properties of cirrus clouds with four different in situ probes: Evidence of small ice crystals, Geophys. Res. Lett., 29, 2230, doi:10.1029/2001gl014342, 2002.
Gayet, J. F., Ovarlez, J., Shcherbakov, V., Ström, J., Schumann, U., Minikin, A., Auriol, F., Petzold, A., and Monier, M.: Cirrus cloud microphysical and optical properties at southern and northern midlatitudes during the INCA experiment, J. Geophys. Res., 109, D20206, doi:10.1029/2004jd004803, 2004.
Gayet, J. F., Shcherbakov, V., Mannstein, H., Minikin, A., Schumann, U., Ström, J., Petzold, A., Ovarlez, J., and Immler, F.: Microphysical and optical properties of midlatitude cirrus clouds observed in the southern hemisphere during INCA, Q. J. Roy. Meteorol. Soc., 132, 2719–2748, doi:10.1256/Qj.05.162, 2006.
Gettelman, A., Morrison, H., and Ghan, S. J.: A new two-moment bulk stratiform cloud microphysics scheme in the community atmosphere model, version 3 (CAM3). Part II: Single-colunm and global results, J. Climate, 21, 3660–3679, 2008.
Ghan, S., Laulainen, N., Easter, R., Wagener, R., Nemesure, S., Chapman, E., Zhang, Y., and Leung, R.: Evaluation of aerosol direct radiative forcing in MIRAGE, J. Geophys. Res., 106,

5295–5316, 2001.
Gierens, K.: On the transition between heterogeneous and homogeneous freezing, Atmos. Chem. Phys., 3, 437–446, 2003, http://www.atmos-chem-phys.net/3/437/2003/.
Ginoux, P., Chin, M., Tegen, I., Prospero, J. M., Holben, B., Dubovik, O., and Lin, S. J.: Sources and distributions of dust aerosols simulated with the GOCART model, J. Geophys. Res., 106, 20255–20273, 2001.
Gong, S. L., Barrie, L. A., and Blanchet, J. P.: Modeling sea-salt aerosols in the atmosphere .1. Model development, J. Geophys. Res., 102, 3805–3818, 1997.
Grabowski, W. W.: Cloud microphysics and the tropical climate: Cloud-resolving model perspective, J. Climate, 13, 2306–2322, 2000.
Greenwald, T. J., Stephens, G. L., Vonderhaar, T. H., and Jackson, D. L.: A physical retrieval of cloud liquid water over the global oceans using special sensor microwave imager (SSM/I) observations, J. Geophys. Res., 98, 18471–18488, 1993.
Haag, W., Kärcher, B., Ström, J., Minikin, A., Lohmann, U., Ovarlez, J., and Stohl, A.: Freezing thresholds and cirrus cloud formation mechanisms inferred from in situ measurements of relative humidity, Atmos. Chem. Phys., 3, 1791–1806, 2003, http://www.atmos-chem-phys.net/3/1791/2003/.
Haag, W. and Kärcher, B.: The impact of aerosols and gravity waves on cirrus clouds at midlatitudes, J. Geophys. Res., 109, D12202, doi:10.1029/2004JD004579, 2004.
Hall, W. D. and Pruppacher, H. R.: Survival of Ice Particles Falling from Cirrus Clouds in Subsaturated Air, J. Atmos. Sci., 33, 1995–2006, 1976.
Han, Q. Y., Rossow, W. B., and Lacis, A. A.: Near-Global survey of effective droplet radii in liquid water clouds using ISCCP data, J. Climate, 7, 465–497, 1994.
Han, Q. Y., Rossow, W. B., Chou, J., and Welch, R. M.: Global variation of column droplet concentration in low-level clouds, Geophys. Res. Lett., 25, 1419–1422, 1998.
Hendricks, J., Kärcher, B., Döpelheuer, A., Feichter, J., Lohmann, U., and Baumgardner, D.: Simulating the global atmospheric black carbon cycle: a revisit to the contribution of aircraft emissions, Atmos. Chem. Phys., 4, 2521–2541, 2004, http://www.atmos-chem-phys.net/4/2521/2004/.
Hendricks, J., Kärcher, B., Lohmann, U., and Ponater, M.: Do aircraft black carbon emissions affect cirrus clouds on the global scale?, Geophys. Res. Lett., 32, L12814, doi:10.1029/2005gl022740, 2005.
Heymsfield, A. J.: Precipitation development in stratiform ice clouds - microphysical and dy-

namical study, J. Atmos. Sci., 34, 367–381, 1977.
Heymsfield, A. J. and Sabin, R. M.: Cirrus crystal nucleation by homogeneous freezing of solution droplets, J. Atmos. Sci., 46, 2252–2264, 1989.
Hoyle, C. R., Luo, B. P., and Peter, T.: The origin of high ice crystal number densities in cirrus clouds, J. Atmos. Sci., 62, 2568–2579, 2005.
Immler, F., Krüger, K., Fujiwara, M., Verver, G., Rex, M., and Schrems, O.: Correlation between equatorial Kelvin waves and the occurrence of extremely thin ice clouds at the tropical tropopause, Atmos. Chem. Phys., 8, 4019–4026, 2008, http://www.atmos-chem-phys.net/8/4019/2008/.
Ito, A. and Penner, J. E.: Historical emissions of carbonaceous aerosols from biomass and fossil fuel burning for the period 1870-2000, Global Biogeochem. Cy., 19, GB2028, doi:10.1029/2004GB002374, 2005.
Jensen, E. J., Toon, O. B., Westphal, D. L., Kinne, S., and Heysmfield, A. J.: Microphysical modeling of cirrus.1. Comparison with 1986 FIRE IFO measurements, J. Geophys. Res., 99, 10421–10442, 1994.
Jensen, E. J. and Toon, O. B.: The potential impact of soot particles from aircraft exhaust on cirrus clouds, Geophys. Res. Lett., 24, 249–252, 1997.
Jensen, E. and Pfister, L.: Transport and freeze-drying in the tropical tropopause layer, J. Geophys. Res., 109, D02207, doi:10.1029/2003JD004022, 2004.
Jensen, E. J., Pfister, L., Bui, T. V., Lawson, P., Baker, B., Mo, Q., Baumgardner, D., Weinstock, E. M., Smith, J. B., Moyer, E. J., Hanisco, T. F., Sayres, D. S., Clair, J. M. St., Alexander, M. J., Toon, O. B., and Smith, J. A.: Formation of large ($\simeq$100 μm) ice crystals near the tropical tropopause, Atmos. Chem. Phys., 8, 1621–1633, 2008, http://www.atmos-chem-phys.net/8/1621/2008/.
Kärcher, B. and Lohmann, U.: A parameterization of cirrus cloud formation: Homogeneous freezing of supercooled aerosols, J. Geophys. Res., 107, 4010, doi:10.1029/2001jd000470, 2002.
Kärcher, B. and Ström, J.: The roles of dynamical variability and aerosols in cirrus cloud formation, Atmos. Chem. Phys., 3, 823–838, 2003, http://www.atmos-chem-phys.net/3/823/2003/.
Kärcher, B., Hendricks, J., and Lohmann, U.: Physically based parameterization of cirrus cloud formation for use in global atmospheric models, J. Geophys. Res., 111, D01205, doi:10.1029/2005JD006219, 2006.
Kärcher, B. and Burkhardt, U.: A cirrus cloud scheme for general circulation models, Q. J. Roy.

Meteorol. Soc., 134, 1439–1461, doi:10.1002/Qj.301, 2008.
Kettle, A. J. and Andreae, M. O.: Flux of dimethylsulfide from the oceans: A comparison of updated data seas and flux models, J. Geophys. Res., 105, 26793–26808, 2000.
Khvorostyanov, V. I., Morrison, H., Curry, J. A., Baumgardner, D., and Lawson, P.: High supersaturation and modes of ice nucleation in thin tropopause cirrus: Simulation of the 13 July 2002 Cirrus Regional Study of Tropical Anvils and Cirrus Layers case, J. Geophys. Res., 111, D02201, doi:10.1029/2004JD005235, 2006.
Kiehl, J. T. and Trenberth, K. E.: Earth's annual global mean energy budget, B. Am. Meteor. Soc., 78, 197–208, 1997.
King, M. D., Menzel, W. P., Kaufman, Y. J., Tanre, D., Gao, B. C., Platnick, S., Ackerman, S. A., Remer, L. A., Pincus, R., and Hubanks, P. A.: Cloud and aerosol properties, precipitable water, and profiles of temperature and water vapor from MODIS, IEEE T. Geosci. Remote, 41, 442–458, doi:10.1109/Tgrs.2002.808226, 2003.
Kinne, S., Schulz, M., Textor, C., Guibert, S., Balkanski, Y., Bauer, S. E., Berntsen, T., Berglen, T. F., Boucher, O., Chin, M., Collins, W., Dentener, F., Diehl, T., Easter, R., Feichter, J., Fillmore, D., Ghan, S., Ginoux, P., Gong, S., Grini, A., Hendricks, J., Herzog, M., Horowitz, L., Isaksen, I., Iversen, T., Kirkevåg, A., Kloster, S., Koch, D., Kristjansson, J. E., Krol, M., Lauer, A., Lamarque, J. F., Lesins, G., Liu, X., Lohmann, U., Montanaro, V., Myhre, G., Penner, J., Pitari, G., Reddy, S., Seland, O., Stier, P., Takemura, T., and Tie, X.: An AeroCom initial assessment – optical properties in aerosol component modules of global models, Atmos. Chem. Phys., 6, 1815–1834, 2006, http://www.atmos-chem-phys.net/6/1815/2006/.
Koop, T., Luo, B. P., Tsias, A., and Peter, T.: Water activity as the determinant for homogeneous ice nucleation in aqueous solutions, Nature, 406, 611–614, 2000.
Krämer, M., Schiller, C., Afchine, A., Bauer, R., Gensch, I., Mangold, A., Schlicht, S., Spelten, N., Sitnikov, N., Borrmann, S., de Reus, M., and Spichtinger, P.: Ice supersaturations and cirrus cloud crystal numbers, Atmos. Chem. Phys., 9, 3505–3522, 2009, http://www.atmos-chem-phys.net/9/3505/2009/.
Lee, D. S., Owen, B., Graham, A., Fichter, C., Lim, L. L., and Dimitriu, D.: Study of the allocation of aviation emissions from scheduled air traffic – present day and historical, Final Report to DEFRA Global Atmosphere Division, Manchester Metropolitan University, 62 pp., online available at: Available from http://www.cate.mmu.ac.uk/project_view.asp?chg=projects&chg2=2&d=2⟩http://www.cate.mmu.ac.uk/project_view.asp?chg=projects&chg2=2&id=2, 2005.

Li, J. L., Waliser, D. E., Jiang, J. H., Wu, D. L., Read, W., Waters, J. W., Tompkins, A. M., Donner, L. J., Chern, J. D., Tao, W. K., Atlas, R., Gu, Y., Liou, K. N., Del Genio, A., Khairoutdinov, M., and Gettelman, A.: Comparisons of EOS MLS cloud ice measurements with ECMWF analyses and GCM simulations: Initial results, Geophys. Res. Lett., 32, L18710, doi:10.1029/2005GL023788 2005.

Liu, X. H. and Penner, J. E.: Effect of Mount Pinatubo H2SO4/H2O aerosol on ice nucleation in the upper troposphere using a global chemistry and transport model, J. Geophys. Res., 107, 4141, doi:10.1029/2001JD000455, 2002.

Liu, X. H. and Penner, J. E.: Ice nucleation parameterization for global models, Meteor. Z., 14, 499–514, doi:10.1127/0941-2948/2005/0059, 2005.

Liu, X., Penner, J. E., Ghan, S. J., and Wang, M.: Inclusion of ice microphysics in the NCAR community atmospheric model version 3 (CAM3), J. Climate, 20, 4526–4547, 2007.

Liu, X. H., Xie, S. C., and Ghan, S. J.: Evaluation of a new mixed-phase cloud microphysics parameterization with CAM3 single-column model and M-PACE observations, Geophys. Res. Lett., 34, L23712 doi:10.1029/2007GL031446, 2007.

Liu, X. H., Penner, J. E., and Wang, M. H.: Influence of anthropogenic sulfate and black carbon on upper tropospheric clouds in the NCAR CAM3 model coupled to the IMPACT global aerosol model, J. Geophys. Res., 114, D03204, doi:10.1029/2008JD010492 2009.

Lohmann, U., Feichter, J., Chuang, C. C., and Penner, J. E.: Prediction of the number of cloud droplets in the ECHAM GCM, J. Geophys. Res., 104, 9169–9198, 1999.

Lohmann, U. and Kärcher, B.: First interactive simulations of cirrus clouds formed by homogeneous freezing in the ECHAM general circulation model, J. Geophys. Res., 107, 4105, doi:10.1029/2001JD000767, 2002.

Lohmann, U., Stier, P., Hoose, C., Ferrachat, S., Kloster, S., Roeckner, E., and Zhang, J.: Cloud microphysics and aerosol indirect effects in the global climate model ECHAM5-HAM, Atmos. Chem. Phys., 7, 3425–3446, 2007, http://www.atmos-chem-phys.net/7/3425/2007/.

Mace, G. G., Clothiaux, E. E., and Ackerman, T. P.: The composite characteristics of cirrus clouds: Bulk properties revealed by one year of continuous cloud radar data, J. Climate, 14, 2185–2203, 2001.

Marcolli, C., Gedamke, S., Peter, T., and Zobrist, B.: Efficiency of immersion mode ice nucleation on surrogates of mineral dust, Atmos. Chem. Phys., 7, 5081–5091, 2007, http://www.atmos-chem-phys.net/7/5081/2007/.

Meyers, M. P., DeMott, P. J., and Cotton, W. R.: New primary ice nucleation parameterizations

in an explicit cloud model, J. Appl. Meteorol., 31, 708–721, 1992.
Mitchell, D. L., Rasch, P., Ivanova, D., McFarquhar, G., and Nousiainen, T.: Impact of small ice crystal assumptions on ice sedimentation rates in cirrus clouds and GCM simulations, Geophys. Res. Lett., 35, L09806, doi:10.1029/2008GL033552 2008.
Möhler, O., Field, P. R., Connolly, P., Benz, S., Saathoff, H., Schnaiter, M., Wagner, R., Cotton, R., Krämer, M., Mangold, A., and Heymsfield, A. J.: Efficiency of the deposition mode ice nucleation on mineral dust particles, Atmos. Chem. Phys., 6, 3007–3021, 2006, http://www.atmos-chem-phys.net/6/3007/2006/.
Murphy, D. M. and Koop, T.: Review of the vapour pressures of ice and supercooled water for atmospheric applications, Q. J. Roy. Meteorol. Soc., 131, 1539–1565, doi:10.1256/Qj.04.94, 2005.
Penner, J. E., Andreae, M. O., Annegarn, H., Barrie, L., Feichter, J., Hegg, D., Jayaraman, A., Leaitch, R., Murphy, D., Nganga, J., and Pitari, G.: Aerosols, their Direct and Indirect Effects, in: Climate Change 2001: The Scientific Basis, Contribution of working group I to the Third Assessment Report of the Intergovernmental Panel on Climate Change, edited by: Houghton, J. T., Ding, Y., Griggs, D. J., Noguer, M., Van der Linden, P. J., Dai, X., Maskell, K., and Johnson, C. A., Cambridge University Press, New York, 881, 2001.
Penner, J. E., Chen, Y., Wang, M., and Liu, X.: Possible influence of anthropogenic aerosols on cirrus clouds and anthropogenic forcing, Atmos. Chem. Phys., 9, 879–896, 2009, http://www.atmos-chem-phys.net/9/879/2009/.
Petzold, A. and Schröder, F. P.: Jet engine exhaust aerosol characterization, Aerosol Sci. Tech., 28, 62–76, 1998.
Phillips, V. T. J., DeMott, P. J., and Andronache, C.: An empirical parameterization of heterogeneous ice nucleation for multiple chemical species of aerosol, J. Atmos. Sci., 65, 2757–2783, doi:10.1175/2007jas2546.1, 2008.
Platnick, S., King, M. D., Ackerman, S. A., Menzel, W. P., Baum, B. A., Riedi, J. C., and Frey, R. A.: The MODIS cloud products: Algorithms and examples from Terra, IEEE T. Geosci. Remote, 41, 459–473, 2003.
Pruppacher, H. R. and Klett, J. D.: Microphysics of Cloud and Precipitation, Springer, New York, 954 pp., 1997.
Pusechel, R. F., Blake, D. F., Snetsinger, K. G., Hansen, A. D. A., Verma, S., and Kato, K.: Black carbon (Soot) aerosol in the lower stratosphere and upper troposphere, Geophys. Res. Lett., 19, 1659–1662, 1992.

Quaas, J., Boucher, O., and Breon, F. M.: Aerosol indirect effects in POLDER satellite data and the Laboratoire de Meteorologie Dynamique-Zoom (LMDZ) general circulation model, J. Geophys. Res., 109, D08205, doi:10.1029/2003jd004317, 2004.

Quaas, J., Boucher, O., and Lohmann, U.: Constraining the total aerosol indirect effect in the LMDZ and ECHAM4 GCMs using MODIS satellite data, Atmos. Chem. Phys., 6, 947–955, 2006, http://www.atmos-chem-phys.net/6/947/2006/.

Quinn, P. K. and Coffman, D. J.: Local closure during the First Aerosol Characterization Experiment (ACE 1): Aerosol mass concentration and scattering and backscattering coefficients, J. Geophys. Res., 103, 16575–16596, 1998.

Ramanathan, V. and Collins, W.: Thermodynamic regulation of ocean warming by cirrus clouds deduced from observations of the 1987 El-Nino, Nature, 351, 27–32, 1991.

Rasch, P. J. and Kristjansson, J. E.: A comparison of the CCM3 model climate using diagnosed and predicted condensate parameterizations, J. Climate, 11, 1587–1614, 1998.

Raval, A. and Ramanathan, V.: Observational determination of the greenhouse-effect, Nature, 342, 758–761, 1989.

Read, W. G., Waters, J. W., Wu, D. L., Stone, E. M., Shippony, Z., Smedley, A. C., Smallcomb, C. C., Oltmans, S., Kley, D., Smit, H. G. J., Mergenthaler, J. L., and Karki, M. K.: UARS microwave limb sounder upper tropospheric humidity measurement: Method and validation, J. Geophys. Res., 106, 32207–32258, 2001.

Rossow, W. B. and Schiffer, R. A.: Advances in understanding clouds from ISCCP, B. Amer. Meteor. Soc., 80, 2261–2287, 1999.

Rotstayn, L. D., Ryan, B. F., and Katzfey, J. J.: A scheme for calculation of the liquid fraction in mixed-phase stratiform clouds in large-scale models, Mon. Weather Rev., 128, 1070–1088, 2000.

Rotstayn, L. D. and Liu, Y. G.: Sensitivity of the first indirect aerosol effect to an increase of cloud droplet spectral dispersion with droplet number concentration, J. Climate, 16, 3476–3481, 2003.

Rotstayn, L. D., Cai, W. J., Dix, M. R., Farquhar, G. D., Feng, Y., Ginoux, P., Herzog, M., Ito, A., Penner, J. E., Roderick, M. L., and Wang, M. H.: Have Australian rainfall and cloudiness increased due to the remote effects of Asian anthropogenic aerosols?, J. Geophys. Res., 112, D09202, doi:10.1029/2006jd007712, 2007.

Sanderson, B. M., Piani, C., Ingram, W. J., Stone, D. A., and Allen, M. R.: Towards constraining climate sensitivity by linear analysis of feedback patterns in thousands of perturbed-physics

GCM simulations, Clim. Dynam., 30, 175–190, 2008.
Schroder, F., Kärcher, B., Duroure, C., Ström, J., Petzold, A., Gayet, J. F., Strauss, B., Wendling, P., and Borrmann, S.: On the transition of contrails into cirrus clouds, J. Atmos. Sci., 57, 464–480, 2000.
Schulz, M., Textor, C., Kinne, S., Balkanski, Y., Bauer, S., Berntsen, T., Berglen, T., Boucher, O., Dentener, F., Guibert, S., Isaksen, I. S. A., Iversen, T., Koch, D., Kirkevåg, A., Liu, X., Montanaro, V., Myhre, G., Penner, J. E., Pitari, G., Reddy, S., Seland, Ø., Stier, P., and Takemura, T.: Radiative forcing by aerosols as derived from the AeroCom present-day and pre-industrial simulations, Atmos. Chem. Phys., 6, 5225–5246, 2006, http://www.atmos-chem-phys.net/6/5225/2006/.
Seifert, M., Ström, J., Krejci, R., Minikin, A., Petzold, A., Gayet, J.-F., Schumann, U., and Ovarlez, J.: In-situ observations of aerosol particles remaining from evaporated cirrus crystals: Comparing clean and polluted air masses, Atmos. Chem. Phys., 3, 1037–1049, 2003, http://www.atmos-chem-phys.net/3/1037/2003/.
Smith, W. L., Ackerman, S., Revercomb, H., Huang, H., DeSlover, D. H., Feltz, W., Gumley, L., and Collard, A.: Infrared spectral absorption of nearly invisible cirrus clouds, Geophys. Res. Lett., 25, 1137–1140, 1998.
Smith, S. J., Pitcher, H., and Wigley, T. M. L.: Global and regional anthropogenic sulfur dioxide emissions, Global Planet. Change, 29, 99–119, 2001.
Smith, S., Andres, R., Conception, L., and Lurz, J.: Historical sulfur dioxide emissions 1850–2000: Methods and resutls, JGCRI Research report PNNL 14537, Paciific Northwest National Laboratory, Richland, WA, USA14537, 16, 2004.
Spichtinger, P., Gierens, K., and Read, W.: The global distribution of ice-supersaturated regions as seen by the Microwave Limb Sounder, Q. J. Roy. Meteorol. Soc., 129, 3391–3410, 2003.
Spichtinger, P., Gierens, K., Smit, H. G. J., Ovarlez, J., and Gayet, J.-F.: On the distribution of relative humidity in cirrus clouds, Atmos. Chem. Phys., 4, 639–647, 2004, http://www.atmos-chem-phys.net/4/639/2004/.
Stephens, G. L., Tsay, S. C., Stackhouse, P. W., and Flatau, P. J.: The relevance of the microphysical and radiative properties of cirrus clouds to climate and climatic feedback, J. Atmos. Sci., 47, 1742–1753, 1990.
Storelvmo, T., Kristjansson, J. E., and Lohmann, U.: Aerosol influence on mixed-phase clouds in CAM-Oslo, J. Atmos. Sci., 65, 3214–3230, doi:10.1175/2008jas2430.1, 2008.
Ström, J. and Heintzenberg, J.: Water-vapor, condensed Water, and crystal concentration in

orographically influenced cirrus clouds, J. Atmos. Sci., 51, 2368–2383, 1994.
Ström, J., Strauss, B., Anderson, T., Schroder, F., Heintzenberg, J., and Wendling, P.: In situ observations of the microphysical properties of young cirrus clouds, J. Atmos. Sci., 54, 2542–2553, 1997.
Ström, J. and Ohlsson, S.: In situ measurements of enhanced crystal number densities in cirrus clouds caused by aircraft exhaust, J. Geophys. Res., 103, 11355–11361, 1998.
Ström, J. and Ohlsson, S.: Real-time measurement of absorbing material in contrail ice using a counterflow virtual impactor, J. Geophys. Res., 103, 8737–8741, 1998.
Ström, J., Seifert, M., Kärcher, B., Ovarlez, J., Minikin, A., Gayet, J.-F., Krejci, R., Petzold, A., Auriol, F., Haag, W., Busen, R., Schumann, U., and Hansson, H. C.: Cirrus cloud occurrence as function of ambient relative humidity: a comparison of observations obtained during the INCA experiment, Atmos. Chem. Phys., 3, 1807–1816, 2003, http://www.atmos-chem-phys.net/3/1807/2003/.
Textor, C., Schulz, M., Guibert, S., Kinne, S., Balkanski, Y., Bauer, S., Berntsen, T., Berglen, T., Boucher, O., Chin, M., Dentener, F., Diehl, T., Easter, R., Feichter, H., Fillmore, D., Ghan, S., Ginoux, P., Gong, S., Grini, A., Hendricks, J., Horowitz, L., Huang, P., Isaksen, I., Iversen, I., Kloster, S., Koch, D., Kirkevåg, A., Kristjansson, J. E., Krol, M., Lauer, A., Lamarque, J. F., Liu, X., Montanaro, V., Myhre, G., Penner, J., Pitari, G., Reddy, S., Seland, Ø., Stier, P., Takemura, T., and Tie, X.: Analysis and quantification of the diversities of aerosol life cycles within AeroCom, Atmos. Chem. Phys., 6, 1777–1813, 2006, http://www.atmos-chem-phys.net/6/1777/2006/.
Tiedtke, M.: Representation of clouds in large-scale models, Mon. Weather Rev., 121, 3040–3061, 1993.
Tompkins, A. M., Gierens, K., and Radel, G.: Ice supersaturation in the ECMWF integrated forecast system, Q. J. Roy. Meteorol. Soc., 133, 53–63, 2007.
Waliser, D. E., Li, J. L. F., Woods, C. P., Austin, R. T., Bacmeister, J., Chern, J., Del Genio, A., Jiang, J. H., Kuang, Z. M., Meng, H., Minnis, P., Platnick, S., Rossow, W. B., Stephens, G. L., Sun-Mack, S., Tao, W. K., Tompkins, A. M., Vane, D. G., Walker, C., and Wu, D.: Cloud ice: A climate model challenge with signs and expectations of progress, J. Geophys. Res., 114, D00A21, doi:10.1029/2008JD010015, 2009.
Wang, P. H., Minnis, P., McCormick, M. P., Kent, G. S., and Skeens, K. M.: A 6-year climatology of cloud occurrence frequency from stratospheric aerosol and gas experiment II observations (1985–1990), J. Geophys. Res., 101, 29407–29429, 1996.

ACPD
9, 16607–16682, 2009

Wang, M. and Penner, J. E.: Aerosol indirect forcing in a global model with particle nucleation, Atmos. Chem. Phys., 9, 239–260, 2009, http://www.atmos-chem-phys.net/9/239/2009/.

Wang, M. H., Penner, J. E., and Liu, X. H.: Coupled IMPACT aerosol and NCAR CAM3 model: Evaluation of predicted aerosol number and size distribution, J. Geophys. Res., 114, D06302, doi:10.1029/2008jd010459, 2009.

Weng, F. Z. and Grody, N. C.: Retrieval of cloud liquid water using the Special Sensor Microwave Imager (SSM/I), J. Geophys. Res., 99, 25535–25551, 1994.

Wu, X. Q.: Effects of ice microphysics on tropical radiative-convective-oceanic quasi-equilibrium states, J. Atmos. Sci., 59, 1885–1897, 2002.

Wu, D. L., Jiang, J. H., and Davis, C. P.: EOS MLS cloud ice measurements and cloudy-sky radiative transfer model, IEEE T. Geosci. Remote, 44, 1156–1165, 2006.

Wu, D. L., Austin, R. T., Deng, M., Durden, S. L., Heymsfield, A. J., Jiang, J. H., Lambert, A., Li, J.-L., Livesey, N. J., McFarquhar, G. M., Pittman, J. V., Stephens, G. L., Tanelli, S., Vane, D. G., and Waliser, D. E.: Comparisons of global cloud ice from MLS, CloudSat, and correlative data sets, J. Geophys. Res., 114, D00A24, doi:10.1029/2008JD009946, 2009.

Wylie, D. P. and Menzel, W. P.: Eight years of high cloud statistics using HIRS, J. Climate, 12, 170–184, 1999.

Xie, S. C., Boyle, J., Klein, S. A., Liu, X. H., and Ghan, S.: Simulations of Arctic mixed-phase clouds in forecasts with CAM3 and AM2 for M-PACE, J. Geophys. Res., 113, D04211, doi:10.1029/2007JD009225, 2008.

Zhang, M. H., Lin, W. Y., Bretherton, C. S., Hack, J. J., and Rasch, P. J.: A modified formulation of fractional stratiform condensation rate in the NCAR Community Atmospheric Model (CAM2), J. Geophys. Res., 108, 4035, doi:10.1029/2002JD002523, 2003.

Zobrist, B., Koop, T., Luo, B. P., Marcolli, C., and Peter, T.: Heterogeneous ice nucleation rate coefficient of water droplets coated by a nonadecanol monolayer, J. Phys. Chem. C, 111, 2149–2155, doi:10.1021/Jp066080w, 2007.

Table 1. Descriptions of simulations.

Case names	Descriptions
HOM	Homogeneous freezing on sulfate particles.
HMHT_0.01IN	Same as HOM, but 1% of soot and dust particles are included to act as heterogeneous IN.
HMHT_0.1IN	Same as HMHT_0.01IN, but 10% of soot and dust particles acts as heterogeneous IN.
HMHT_1IN	Same as HMHT_0.01IN, but 100% of soot and dust particles act as heterogeneous IN.
HMHT_0.75dT	Same as HMHT_0.01IN, but temperature perturbation is decreased by 25%.
HMHT_1.25dT	Same as HMTH_0.01IN, but temperature perturbation is increased by 25%.

ACPD
9, 16607–16682, 2009

Table 2. Annual global mean cloud properties and their interannual variations (standard deviations).

	HOM	HMHT_0.01IN	HMHT_0.1IN	HMHT_1IN	HMHT_1.25dT	HMHT_0.75T	LIU07	CAM3	Obs
LWP[a]	77.45±0.53	76.44±0.42	75.26±0.15	82.00±0.36	78.15±0.28	75.38±0.65	141	121	50–87
IWP[b]	20.94±0.01	21.03±0.03	21.14±0.07	21.79±0.13	21.39±0.06	20.92±0.06	21.8	15.6	26.7
N_d^c	2.28±0.017	2.24±0.025	2.24±0.009	2.48±0.011	2.32±0.007	2.20±0.09	#	#	4
N_i^c	0.022±9.82e-5	0.016±2.55e-4	0.0085±2.70e-5	0.051±1.47e-3	0.024±5.08e-4	0.0089±2.40e-4	0.027	#	
r_{effi}^c	11.09±0.01	11.10±0.01	11.10±0.02	11.06±0.02	11.08±0.01	11.12±0.01	#	#	11.4–15.7
r_{effi}^d	39.63±0.28	43.91±0.20	43.09±0.19	35.11±0.09	40.99±0.55	47.77±0.13	#	#	25.21
N_{itop}^d	0.28±2.81e-3	0.17±2.10e-3	0.067±6.60e-4	0.50±7.72e-3	0.31±1.65e-3	0.081±1.51e-3		#	
TCC[e]	66.41±0.10	67.33±0.13	68.40±0.08	68.46±0.10	67.14±0.09	68.19±0.14	77.90	58.6	65–67
TCCHGH[e]	35.82±0.12	38.18±0.08	40.22±0.10	39.92±0.16	37.20±0.16	39.60±0.11	56.80	32.2	21
TCCLOW[e]	44.24±0.11	43.87±0.18	43.63±0.02	45.30±0.12	44.50±0.03	43.67±0.11			

[a] The liquid water path (LWP, g/m^2) observations are from SSM/I (for the years 1987–1994, Ferraro et al., 1996; for August 1993 and January 1994, Weng and Grody, 1994; and for August 1987 and February 1988, Greenwald et al., 1993) and ISCCP for the year 1987 (Han et al., 1994). SSM/I data are restricted to oceans.

[b] Ice water path (IWP, g/m^2) has been derived from ISCCP data for the years 1983–2000 (Storelvmo et al., 2008).

[c] N_d and N_i refer to the vertically integrated cloud droplet and ice crystal number concentration (10^{10} m^{-2}), and r_{effl} (μm) refers to the cloud top effective radius. Observations of N_d are obtained from ISCCP for the year 1987 (Han et al., 1998) and observations of r_{effl} are obtained from ISCCP for the year 1987 (Han et al., 1994) and from MODIS (version 4) for the year 2001 (Platnick et al., 2003), and are limited to 50° N to 50° S.

[d] r_{effi} and N_{itop} refer to ice crystal radius and number at the top of cirrus clouds, respectively. Observations of r_{effi} (μm) and N_{itop} (#/cm^3) are from MODIS data (version 4) for the year 2001.

[e] Total cloud cover (TCC) was obtained from ISCCP for the years 1983–2001 (Rossow and Schiffer, 1999) and MODIS data for the years 2001–2004 (Platnick, 2003). High cloud cover (TCCHGH) was obtained from ISCCP data for the years 1983–2001. TCCLOW refers to low level cloud cover.

ACPD
9, 16607–16682, 2009

Table 3. Annual global mean shortwave cloud forcing (SWCF, W/m^2), longwave cloud forcing (LWCF, W/m^2), net cloud forcing (CF, W/m^2), total precipitation (Ptot, mm/day), water vapor mass (WVM, kg/m^2), net incoming radiation at the top of the atmosphere (FNT, W/m^2), and clear sky net long wave radiation at the top of the atmosphere (FLNTC, W/m^2, negative values mean outgoing) and their interannual variations (standard deviations).

	HOM	HMHT_0.01IN	HMHT_0.1IN	HMHT_1IN	HMHT_1.25dT	HMHT_0.75T	LIU07	CAM3	Obs
SWCF[a]	−52.21±0.12	−51.47±0.31	−50.65±0.12	−55.83±0.24	−52.72±0.04	−50.40±0.25	−59.1	−54.6	−47 to −54
LWCF[a]	27.60±0.07	26.72±0.03	26.22±0.03	31.53±0.13	28.19±0.13	25.43±0.09	31.9	30.6	29 to 30
CF	−24.61±0.16	−24.75±0.20	−24.43±0.10	−24.30±0.22	−24.53±0.15	−24.97±0.17	−27.2	−24.0	
Ptot[b]	2.89±0.001	2.92±0.006	2.94±0.004	2.81±0.005	2.88±0.004	2.96±0.007	#		2.61
WVM[c]	24.42±0.07	24.15±0.03	23.95±0.05	25.26±0.08	24.43±0.06	23.92±0.02			22.80
FNT	2.63±0.05	2.14±0.21	1.71±0.17	3.94±0.21	2.86±0.04	1.59±0.26			
FLNTC	−261.94±0.15	−262.33±0.19	−262.95±0.17	−261.05±0.32	−261.82±0.14	−262.58±0.13			

[a] The shortwave (SWCF) and longwave cloud forcing (LWCF) observations are taken from ERBE for the years 1985–1989 (Kiehl and Trenberth, 1997) and CERES for the years 2000–2005 (http://science.larc.nasa.gov/ceres).

[b] Total precipitation (P_{tot}) observations are taken from the Global Precipitation Data Set for the years 1979–2002 (http://precip.gsfc.nasa.gov).

[c] Water vapor mass (WVM) data is from MODIS for the years 2001–2004 (King et al., 2003).

ACPD
9, 16607–16682, 2009

Table 4. Comparison of measured ice crystal number concentration ("Obs") during the INCA campaign (Gayet et al., 2004) over the SH (Punta Arenas, Chile, in March/April) and over the NH (Prestwick, Scotland, in September/October) with those simulated from the prognostic ice crystal equations in the model (units: #/cm^3).

	HOM[a]	HMHT_ 0.01IN[a]	HMHT_ 0.1IN[a]	HMHT_ 1IN[a]	HMHT_ 1.25dT[a]	HMHT_ 0.75dT[a]	Obs[a]
Chile, SH	0.34 (1.16)[b]	0.32	0.05	0.28	0.43	0.21	1.45 (0.58–3.01)[c]
Scotland, NH	0.33 (1.60)[b]	0.06	0.11	0.58	0.22	0.02	2.23(0.84–4.74)[c]

[a] Median values from the observations are shown. For the model simulations, monthly mean results are used, and are averaged over 60°–50° S, 70°–85° W, from March to May in Chile, and over 50°–60° N, 10° W–5° E, from September to November in Scotland. Model results are restricted to pressure levels from 200 hpa to 300 hPa, and to temperatures from −35°C to −60°C.
[b] Numbers in parentheses are ice crystal number concentrations immediately after the initial homogeneous freezing.
[c] Numbers in parentheses represent 25 to 75 percentile.

ACPD
9, 16607–16682, 2009

Table B1. Size distribution parameters for aerosols.

Aerosol component	Ni	Ri, μm	Sigma
Sulfate[a]	1.0	0.05	1.9
Fossil fuel OM/BC[a]	1.0	0.05	1.9
Biomass OM/BC and natural OM[b]	1.0	0.08	1.65
Sea Salt[c]	0.965	0.035	1.92
	0.035	0.41	1.70
Dust[d]	0.152	0.01	2.3
	0.727	0.045	1.6
	0.121	0.275	2.5

[a] The size distribution of sulfate and internal mixture fossil fuel OM/BC is the fossil fuel size distribution taken from Penner et al. (2001, Table 5.1).
[b] The size distribution of internal mixture biomass burning OM and BC is the biomass burning size distribution from Penner et al. (2001, Table 5.1).
[c] The size distribution of sea slat is taken from Quinn and Coffman (1998).
[d] The size distribution of dust is taken from de Reus et al. (2000).

ACPD
9, 16607–16682, 2009

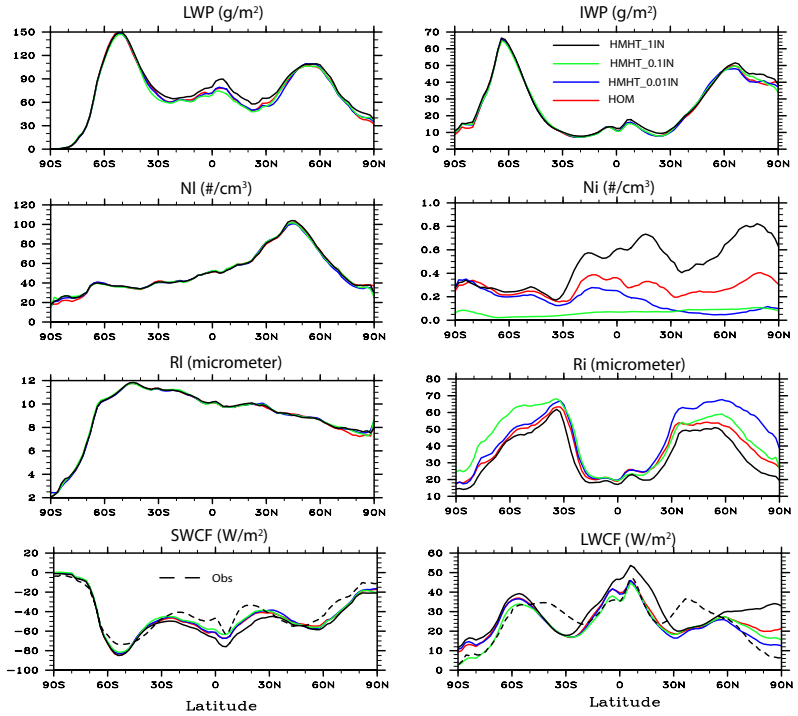

Fig. 1. Annual average zonal mean liquid water path (LWP, g/m^2), ice water path (IWP, g/m^2), cloud top in-cloud liquid droplet number concentration (N_l, #/cm^3), cloud top liquid droplet effective radius (R_l, μm), cirrus cloud top in-cloud ice crystal number (N_i, #/cm^3), and cirrus cloud top ice crystal radius (R_i, μm), shortwave cloud forcing (SWCF, W/m^2), and longwave cloud forcing (LWCF, W/m^2) for four cases: HOM, HMTH_0.01IN, HMHT_0.1IN, HMHT_1IN. For shortwave and long wave cloud forcing, observations from CERES data for the years 2000–2005 (http://science.larc.nasa.gov/ceres) are included as the dashed black line.

ACPD
9, 16607–16682, 2009

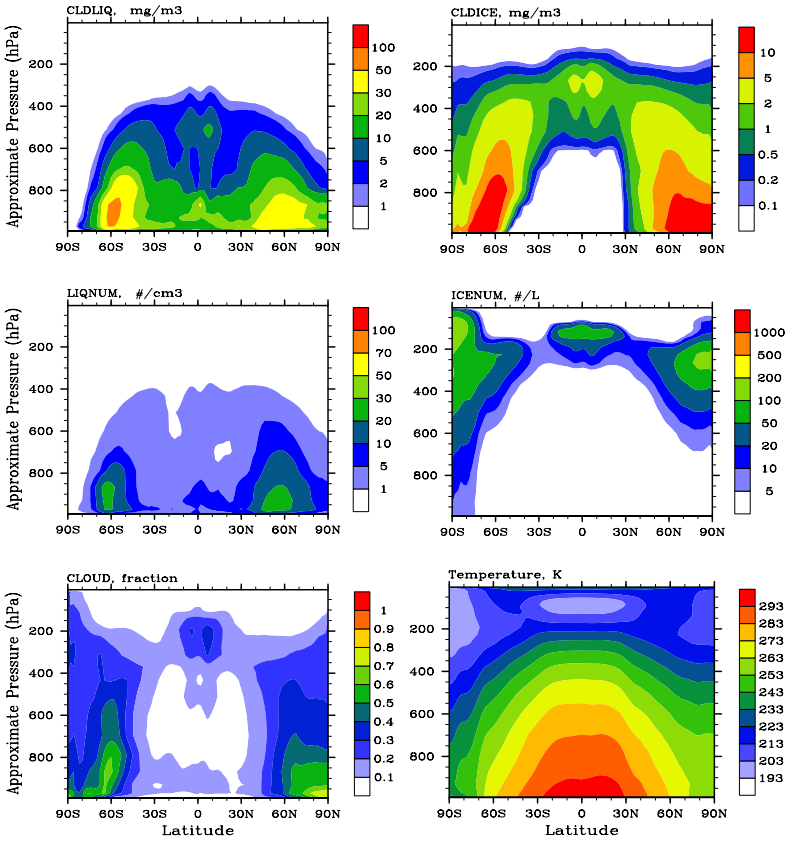

Fig. 2. Annual average zonal mean grid-mean cloud liquid water content (CLDLIQ, mg/m^3), cloud ice water content (CLDICE, mg/m^3), cloud liquid droplet number (LIQNUM, #/cm^3), cloud ice crystal number (ICENUM, #/L), cloud fraction (CLOUD) and temperature (K) for the HOM case.

ACPD
9, 16607–16682, 2009

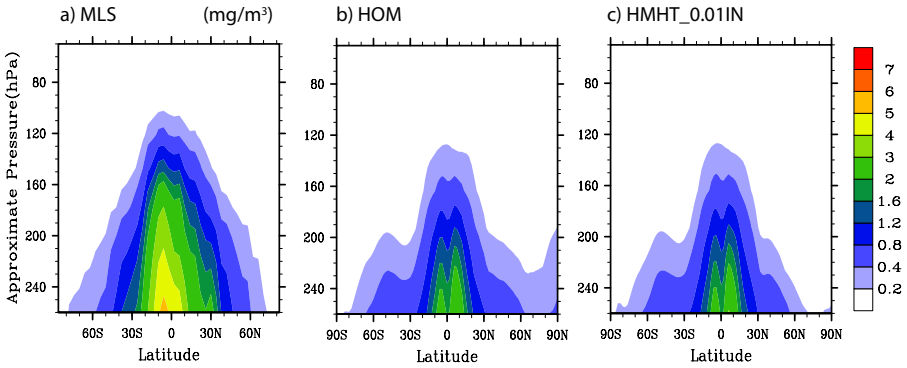

Fig. 3. Annual average zonal mean **(a)** grid-averaged ice water content that measured by the Aura MLS instrument, **(b)** grid-averaged ice water content that predicted in HOM, and **(c)** that predicted in HMHT_0.01IN (mg/m^3).

ACPD
9, 16607–16682, 2009

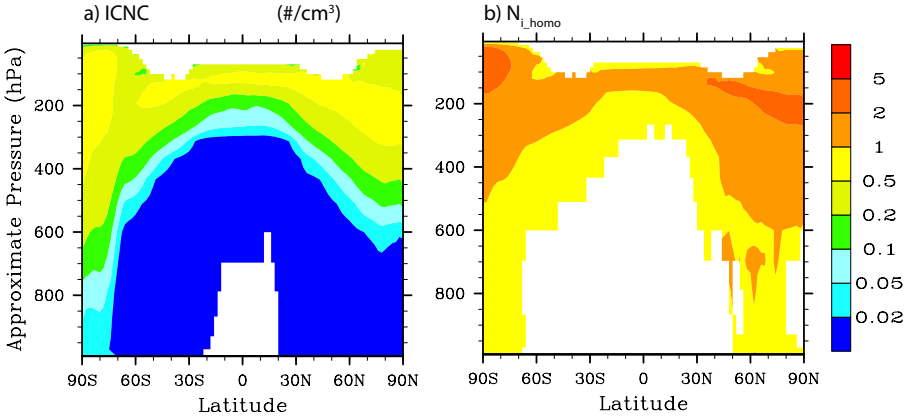

Fig. 4. Annual average zonal mean **(a)** in-cloud ice crystal number concentration (#/cm^3) predicted by the prognostic ice crystal equation and **(b)** that calculated after the initial nucleation in the HOM case.

ACPD
9, 16607–16682, 2009

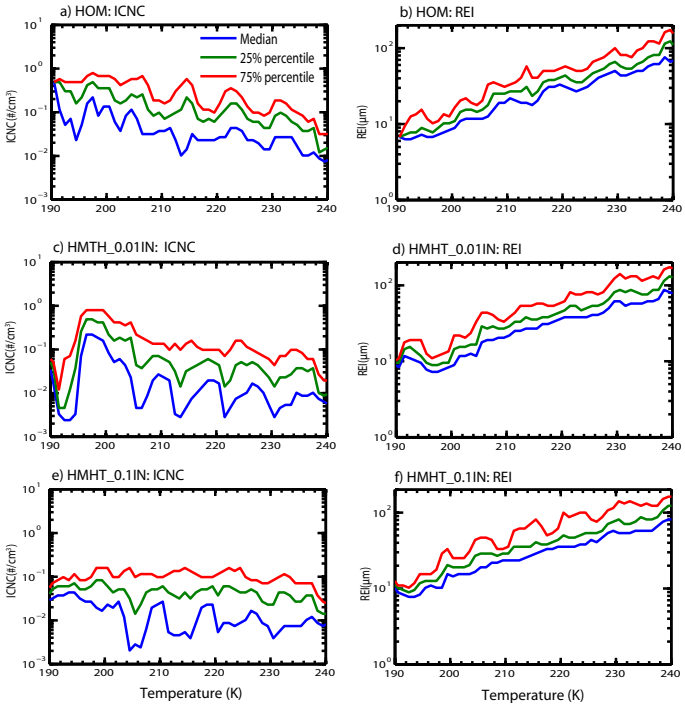

Fig. 5. In-cloud ice crystal number concentration (ICNC, #/cm^3) and ice crystal effective radius (REI, μm) versus temperature. Model results are sampled every six hours over six flight regions (Kiruna, Sweden in January and February; Hohn, Germany in November and December; Forli, Italy in Octorber; Mahe, Seychelles, in February and March; Darwin, Australia, in November; Aracabuta, Brazil in January and February) where the observation reported in Krämer et al. (2009) were collected (See Table 3 in Krämer et al. (2009) for the flight information). The 50 percentile (green line), 25% percentile (blue line), and 75% percentile (red line) are shown for each 1 K temperature bins. The upper panel is for the HOM case; the middle panel is for the HMHT_0.01IN case; and the low panel is for the HMHT_0.1IN case.

ACPD
9, 16607–16682, 2009

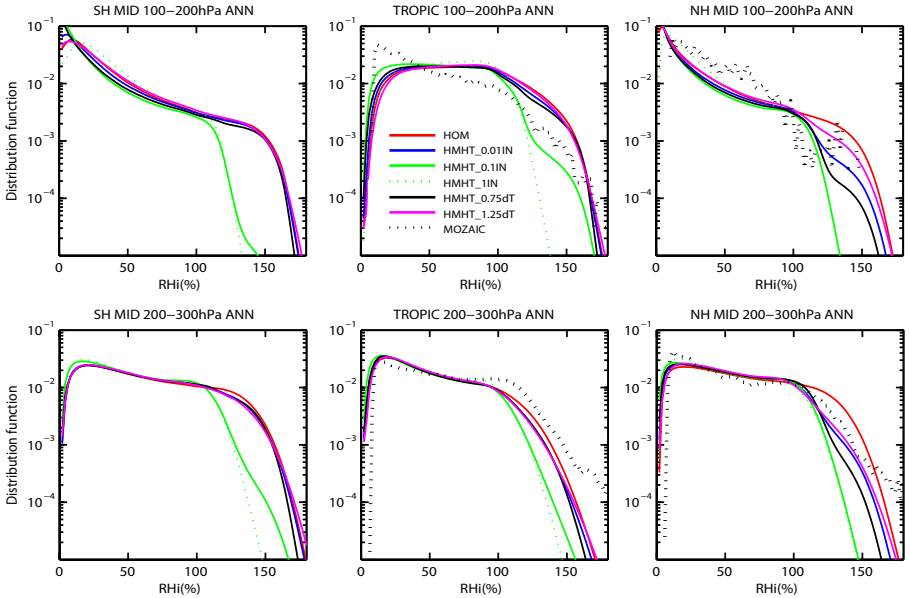

Fig. 6. Frequency of occurrence of RH*i* in the SH middle latitudes (60° S–30° S) (SH MID, left panel), in the tropics (30° S–30° N) (TROPIC, middle panel), and the NH middle latitudes (30° N–60° N) (NH MID, right panel) at 100–200 hPa (upper panel) and at 200–300 hPa (lower panel) from all simulations listed in Table 1. Observations from MOZAIC data in the tropics and in the NH middle latitudes are also shown.

ACPD
9, 16607–16682, 2009

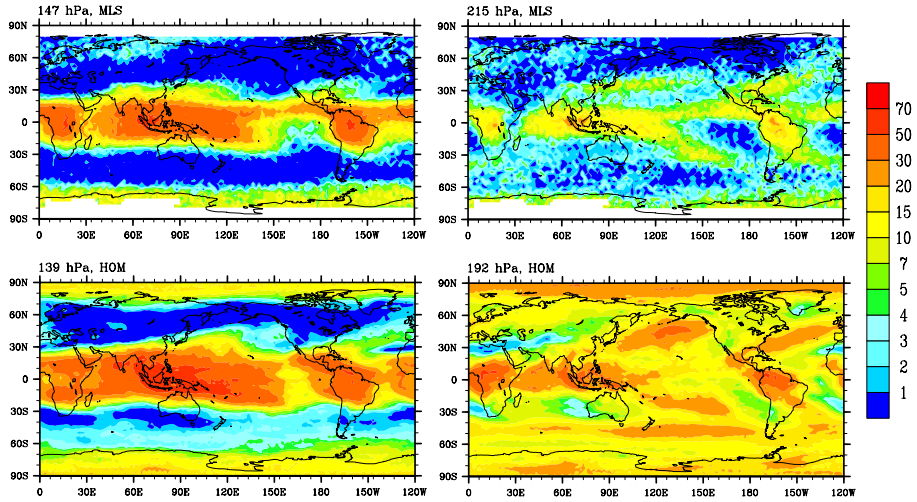

Fig. 7. Annual-average frequency of occurrence of ice supersaturation from MLS data (upper panel) for the HOM case (lower panel) at 147 hPa (139 hPa for the model) (left panel) and 215 hPa (192 hPa for the model) (lower panel).

ACPD
9, 16607–16682, 2009

(a) 149 hPa

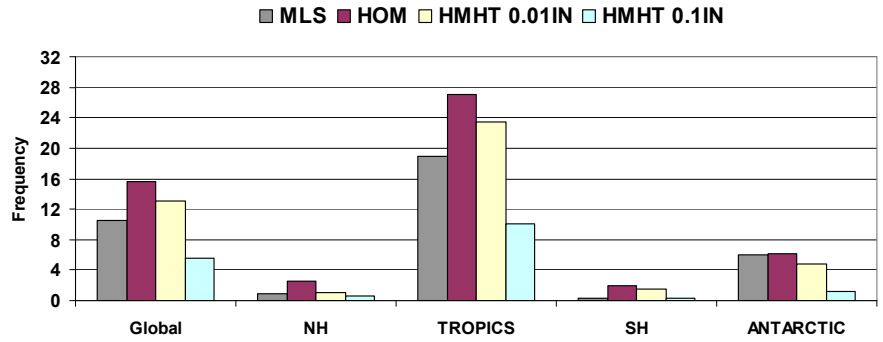

(b) 215 hPa

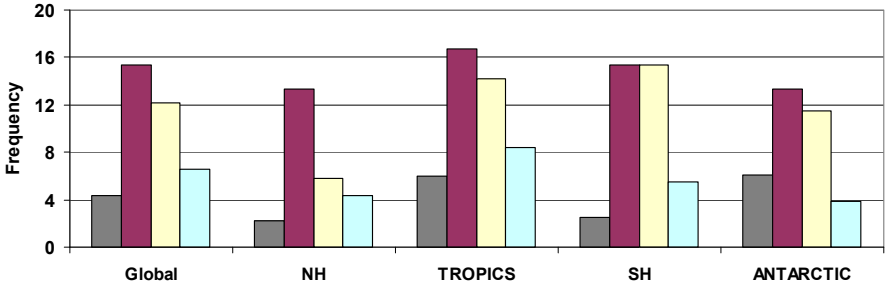

Fig. 8. Regionally-averaged frequency of occurrence of ice supersaturation from MLS data and from three simulations: HOM, HMHT_0.01IN, and HMHT_0.1IN, **(a)** at 149 hPa (139 hPa for the model) and at **(b)** 215 hPa (192 hPa for the model) over five regions: Global (80° S–80° N), NH (Northern Hemisphere, 30° N–80° N), TROPICS (30° N–30° S), SH (Southern Hemisphere, 55° S–30° S), and Antarctic (80° S–55° S).

ACPD
9, 16607–16682, 2009

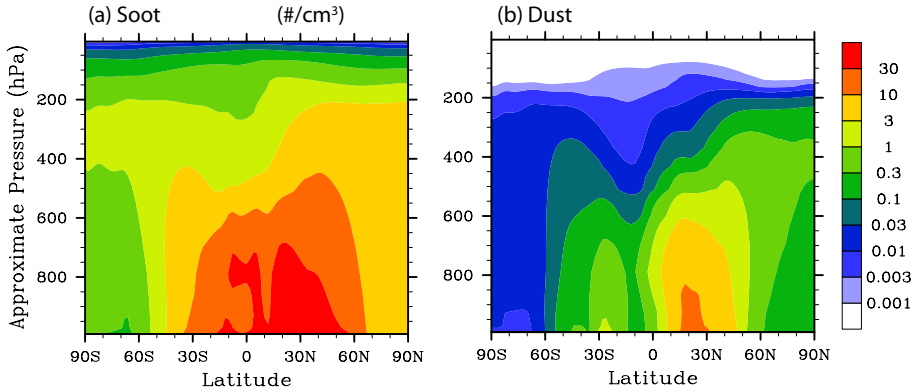

Fig. 9. Annual average zonal mean **(a)** soot and **(b)** dust number concentration (#/cm^3).

ACPD
9, 16607–16682, 2009

Cirrus clouds in a global climate model

M. Wang and
J. E. Penner

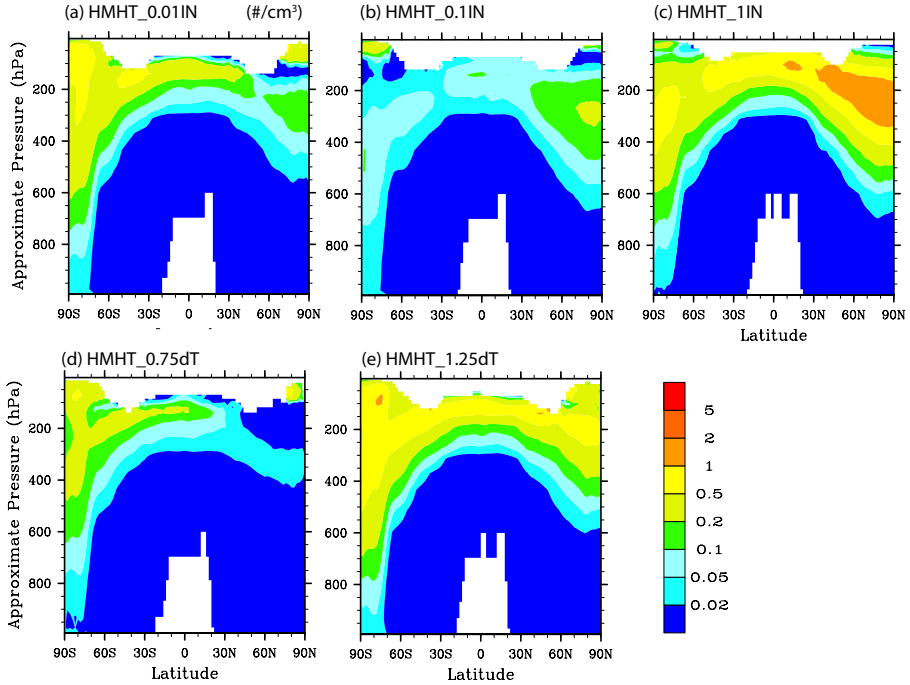

Fig. 10. Annual average zonal mean ice crystal number concentration (#/cm^3) in all five cases that allow the competition between homogeneous freezing and heterogeneous freezing. All cases are described in Table 1.

ACPD
9, 16607–16682, 2009